Geologic and Structural Evolution of the NE Lau Basin, Tonga: Morphotectonic Analysis and Classification of Structures using Shallow Seismicity

Melissa O. Anderson[1†], Chantal Norris-Julseth[1†], Kenneth H. Rubin[2], Karsten Haase[3], Mark D. Hannington[4,5], Alan T. Baxter[4], and Margaret S. Stewart[6]

[1]Department of Earth Sciences, University of Toronto, 22 Ursula Franklin Street, Toronto, Ontario, M5S 3B1, Canada

[2]Department of Geology and Geophysics, SOEST, University of Hawaii, 1680 East-West Road, Honolulu, Hawaii, 96822, USA

[3]GeoZentrum Nordbayern, Friedrich-Alexander University of Erlangen-Nürnberg, Schlossgarten 5, D-91054 Erlangen, Germany

[4]Department of Earth Sciences, University of Ottawa, 25 Templeton, Ottawa, Ontario, K1N 6N5, Canada

[5]GEOMAR, Helmholtz Centre for Ocean Research Kiel, Wischhofstrasse 1-3, 24148 Kiel, Germany

[6]Department of Earth and Environmental Sciences, Mount Royal University, 4825 Mount Royal Gate SW, Calgary, Alberta, T3E 6K5, Canad

*** Correspondence:**
Melissa O. Anderson: melissao.anderson@utoronto.ca

Keywords: NE Lau Basin, backarc basin, geologic mapping, morphotectonic, submarine volcanism, shallow seismicity, fault kinematics, Riedel megashear, hydrothermal systems,

Abstract

The transition from subduction to transform motion along horizontal terminations of trenches is associated with tearing of the subducting slab and strike-slip tectonics in the overriding plate. One prominent example is the northern Tonga subduction zone, where abundant strike-slip faulting in the NE Lau back-arc basin is associated with transform motion along the northern plate boundary and asymmetric slab rollback. Here, we address the fundamental question: how does this subduction-transform motion influence the structural and magmatic evolution of the back-arc region? To answer this, we undertake the first comprehensive study of the geology and geodynamics of this region through analyses of morphotectonics (remote-predictive geologic mapping) and fault kinematics interpreted from ship-based multibeam bathymetry and Centroid-Moment Tensor data. Our results highlight two unique features of the NE Lau Basin: (1) the occurrence of widely distributed off-axis volcanism, in contrast to typical ridge-centered back-arc volcanism, and (2) fault kinematics dominated by shallow-crustal strike slip-faulting (rather than normal faulting) extending over ~120 km from the transform boundary. The orientations of these strike-slip faults are consistent with reactivation of earlier-formed normal faults in a sinistral megashear zone. Notably, two distinct sets of Riedel megashears are identified, indicating a recent counter-clockwise rotation of part of the stress field in the back-arc region closest to the arc. Importantly, these structures directly control the development of complex volcanic-compositional provinces, which are characterized by variably-

oriented spreading centers, off-axis volcanic ridges, extensive lava flows, and point-source rear-arc volcanoes that sample a heterogenous mantle wedge, with sharp gradients and contrasts in composition and magmatic affinity. This study adds to our understanding of the geologic and structural evolution of modern backarc systems, including the association between subduction-transform motions and the siting and style of seafloor volcanism.

1 Introduction

Back-arc basins are extensional features formed behind subduction zones by progressive rifting of volcanic arcs until passive mantle upwelling creates new oceanic crust (Karig, 1970). Their initiation is triggered by processes of either hinge-rollback (Chase, 1978; Scholz and Campos, 1995), and/or slab anchoring on the trenchward side of the upper plate (Heuret and Lallemand, 2005). Once back-arc spreading is established, it may continue regardless of the motion of the overriding plate (Sdrolias and Müller, 2006). Movement of the overriding plate relative to the arc and subduction zone leads to a diverse arrangement of plates and deformation styles within the near-arc and back-arc environments (Heuret and Lallemand, 2005). Edge-driven kinematics are common along the boundaries of microplates, where microplate rotation is driven by the motion of the two larger plates the microplate is pinched between (Schouten et al., 1993). These microplate rotations can cause block rotations, shearing, and further rift propagation (e.g., Easter Microplate: Neves et al., 2003). Hinge-rollback, seamount subduction, microplate interactions, and variations in trench geometry and/or subduction angle all influence the state of stress in the overriding plate, driving upper mantle flow and magmatic upwelling, and the formation of structures that provide pathways for magma to reach the surface. However, seismic data alone cannot fully resolve the types of faulting, and therefore the stress regimes that lead to the emergence of these structures often remain enigmatic.

This paper focuses on the geological and structural evolution of the NE Lau Basin, which is one of the most volcanically- and tectonically-active places on Earth (Embley et al., 2009; Rubin et al., 2013; Embley and Rubin, 2018). New high-resolution multibeam bathymetry collected by the R/V Falkor expedition FK171110 in 2017 and R/V Sonne expedition SO-263 in 2018 are compiled with previously-collected bathymetry, and are used for morphotectonic analyses. Interpretations of this data, together with seafloor samples and ground truthing, are used to create the first remote-predictive geologic and structural maps of the region. The structures are further classified based on shallow seismicity (Centroid Moment Tensors) to provide insight into the recent kinematic evolution of the faulting. This analysis provides context for understanding the controls on the development of large magmatic-hydrothermal systems across the study area.

2 Tectonic Setting

The Tonga-Kermadec subduction zone in the western Pacific extends over 2000 km from New Zealand to Fiji, where the Pacific Plate subducts westward beneath the Indo-Australian Plate (**Fig. 1**). Collision of the Louisville Seamount Chain with the trench has segmented the subduction zone into the Tonga Trench in the north and the Kermadec Trench in the south. This collision induced compression in the fore-arc and may have influenced where and when rifting in the back-arc occurred (Ruellan et al., 2003). Rifting of the Tonga Arc at 5.5–6 Ma formed the Lau Basin (**Fig. 2**), which evolved to mature seafloor spreading at ca. 5 Ma (Wiedicke and Collier, 1993; Taylor et al., 1996). As the Tonga Trench migrated eastward, arc volcanism shifted from the remnant Lau Ridge to form the new Tofua Arc at 3.5 Ma (Tappin et al., 1994). In the southern part of the subduction zone, rifting of the Kermadec Arc at ca. <2 Ma produced the Havre Trough (Wysoczanski et al., 2019).

This is a provisional file, not the final typeset article

The orientation of the modern Tonga Trench is north-easterly, with a sharp bend to a westerly direction at the northern apex where there is a transition from subduction to transform motion (Govers and Wortel, 2005). This boundary is referred to as a Subduction-Transform-Edge-Propagator (STEP) boundary, associated with vertical tearing that causes a piece of the subducting plate to remain at surface (Nijholt and Govers, 2015). Behind the arc, the modern Lau Basin displays a tapering V-shape with a width of ~500 km in the north, narrowing to 200 km in the south where it merges with the Havre Trough at 26°S (**Fig. 2**). In the south, two plates (Tongan and Australian) are separated by a single segmented spreading center. The number of spreading centers increases northward, indicating increasing tectonic complexity (Sleeper and Martinez, 2016). The Niuafo'ou Microplate in the north has been interpreted to occur between the Tongan and Australian plates, although it is bounded by and contains numerous small spreading centers and propagating rifts, and so structurally might be even more complex (i.e., multiple microplates). There are likely several other micro- or nano-plates in the northern basin with poorly defined (possibly diffuse) boundaries (Zellmer and Taylor, 2001; Phillips, 2003; Conder and Wiens, 2011; Baxter et al., 2020).

Plate reconstructions by Sleeper and Martinez (2016) suggest that non-rigid plate behavior may be important in this area, where plate boundaries can propagate and rotate, and experience intraplate deformation. Notably, the NE Lau Basin is dominated by strike-slip faulting, revealed by analysis of focal mechanisms of shallow crustal earthquakes (Hawkins, 1994; Baxter et al., 2020). Baxter et al. (2020) describe these focal mechanisms across the entire Lau Basin, and interpret strike-slip faulting to result from re-activation of normal faults produced along spreading centers. In this study, we focus on the structures of the NE Lau Basin in greater detail, complemented by morphotectonic analyses (remote-predictive geologic mapping), in order to better understand the origin and evolution of strike-slip faulting and the possible influence on back-arc magmatic-hydrothermal processes.

3 Data and Methods

This study combines large hydro-acoustic datasets (multibeam bathymetry and backscatter) and seafloor sampling and observations from the past decade. Interpretation of this data (including morphotectonic analyses) is used to generate a remote-predictive geological map of the study area. This is critical for understanding the controls on the distribution of structural and geologic features. Publicly available Centroid Moment Tensor (CMT) data is interpreted together with the orientations of nearby structures to investigate fault kinematics.

3.1 Bathymetric Data and Remote-Predictive Geologic Mapping

Ship-based multibeam bathymetric data from the NE Lau Basin were collected during two R/V Kilo Moana cruises in 2010 (KM1024; Rubin et al., 2010) and 2011 (KM1129; Martinez et al., 2013), and are supplemented here with new data from R/V Falkor cruise FK171110 in 2017 (Rubin et al., 2018), and R/V Sonne cruise SO-263 in 2018 (Tonga Rift: Haase et al., 2018). The R/V Kilo Moana and R/V Sonne are equipped with Kongsberg EM 122 multibeam echo sounders with operating frequencies of 12 kHz, and the R/V Falkor is equipped with a Kongsberg EM 302 multibeam echo sounder with an operating frequency of 30 kHz. The combined surveyed area is 40,760 km^2, covering 73% of the map area (**Fig. 3**, **Supplementary Fig. S1**). The raw multi-beam data were cleaned and gridded at cell sizes of 30 to 50 m by the various shipboard scientific parties. The data were compiled together with the 2019 GEBCO grid (GEBCO Compilation Group, 2019) and reprocessed using the "Terrain Texture Shading" (TTS) technique developed by Brown (2014) as an interpretive tool in applied geomatics to reveal subtle surface and structural features that can be directly correlated with seafloor geomorphology (e.g., Augustin et al., 2016; Anderson et al. 2016; 2017). Hydroacoustic

backscatter data was also collected during the SO-263 and FK171110 cruises. The intensity of the backscatter signal is an important indicator for the nature of the seafloor, where strong signal returns indicate hard substrates (such as young lava flows), whereas signals become attenuated with increasing sediment cover. Variations in the seafloor rugosity and slope also affect the backscatter signal.

The morphology of the seafloor is characterized by several important factors derived from the bathymetry, including slope, rugosity (or vector ruggedness measure), and aspect, which were explored using the Benthic Terrain Modeler (BTM) 3.0 add on in ArcGIS v.10.6 (**Fig. 3**). The distribution of these morphologic features was interpreted together with backscatter data to define the classification scheme for a remote-predictive geological map, following the criteria outlined by Anderson et al. (2016; 2017) and Klischies et al. (2019). Lithologies were then ascribed to these units based on available data from ROV sampling, TV grabs (visually aided ship-based scoop sampling), and wax coring from the SO-263 cruise and a compilation of data from literature (**Supplementary Fig. S1**). In addition to these morphological/lithological units, fully georeferenced measurements of structural features, including faults, volcanic ridges, and lineaments are interpreted and digitized. Relative ages of the mapped units were established from overlapping and cross-cutting relationships (e.g., if one lava flow onlaps another, or one structure displaces another), and morphological and backscatter evidence of young volcanic flow features and sediment cover.

Further "ground-truthing" of the map legend was provided by seafloor observations during ROV dives; seventeen dives were with the MARUM ROV Quest 4000 during the 2018 SO-263 cruise (Haase et al., 2018), and seven dives from the TN234 cruise using WHOI ROV Jason-2 (five dives at West Mata and two dives on the southern NELSC; Resing et al., 2009). The SO-263 QUEST 4000 dives included one that transected the wall of the graben in the NE map area that hosts the Niua volcano (Escarpment A), one that transected the northern Tonga forearc, six dives at vent sites at the Niua arc volcano, six dives at various locations around Niuatahi volcano, and two dives at the southern NELSC near the Maka seamount and its summit hydrothermal vent site (Haase et al., 2018).

3.2 Shallow Seismicity and Fault Kinematics

Seismic data was collected from the Global Centroid Moment Tensor (GCMT) project (www.globalcmt.org; accessed September 2018) over the study area, filtering for shallow (≤25 km) earthquakes limited to the upper plate and excluding CMTs that may be associated with the down-going slab. All CMTs included in the dataset (n = 174) are large magnitude with Mw > 5.0, and includes values for the strike, dip, and rake of two possible focal planes. To determine the correct focal plane solution, each CMT was interpreted in the context of the dominant lineament orientation (e.g., **Supplementary Fig. S2**), plotted using the ArcBeachball tool (v.2.2). This technique has been used since scientists first started recording seismic moments (e.g., McKenzie, 1969) and is described in detail by Baxter et al. (2020). This data was used for interpretation of fault kinematics and is supplemented by interpretations of offset features where cross-cutting relationships exist.

4 Results: Geological and Structural Features of the NE Lau Basin

Most of the prior work towards understanding the geology of the Lau Basin has been on regional-scale studies of the crustal evolution and shallow seismicity (e.g., Sleeper and Martinez, 2016; Baxter et al., 2020; Stewart et al., in press). Higher-resolution studies have focused on the southern basin along the Eastern and Central Lau Spreading Centers, where crustal accretion resembles mid-ocean ridges. This contrasts the processes of crustal accretion in the NE Lau Basin, where a diffuse system of back-arc extension, short-lived rifts, spreading centers, jumping ridge crests, and point-source

This is a provisional file, not the final typeset article

volcanism dominate (Taylor et al., 1996; Embley et al., 2009). In the study area, there are five distinct crustal types: Lau back-arc crust, Lau rear-arc crust, Tofua arc crust, paleo-arc crust, and Pacific Plate crust (undifferentiated), as shown in **Fig. 4**. Based on detailed morphotectonic analyses and additional ground-truthing data, we present new remote-predictive geological and structural maps of the NE Lau Basin at high-resolution (**Figs. 5–7**; **Supplementary Table S1**), which highlight the wide variety of rock types, extensive volcanism, and complex structural fabrics resulting from the dynamic evolution of the area.

4.1 Lau Back-Arc Crust: Rifts and Spreading Centers

The spreading centers in the study area include the three arms of the Mangatolou Triple Junction (MTJ; formerly the "Kings Triple Junction"), the North-East Lau Spreading Center (NELSC), and the northern half of the Fonualei Rift and Spreading Center (FRSC). The spreading centers primarily erupt basalt, with lesser amounts of basaltic andesite, andesite, rhyolite, and boninite, with distinct geochemical signatures along each spreading center (Falloon et al., 2007; Tian et al., 2011; Escrig et al., 2012; Rubin et al., 2018; Haase et al., 2018). Sampling of the MTJ has revealed a diverse suite of lithologies, spanning the compositional range from basalt to andesite to dacite (Nilsson et al., 1989; Falloon et al., 1992; Hawkins, 1995; Langmuir et al., 2006). The NELSC has a mixed geochemical signature of OIB and N-MORB, in addition to subtle arc-like affinities (Keller et al., 2008; Zhang et al., 2018). Along the southern MTJ arm and the FRSC, IAB signatures are most abundant, with boninitic signatures in the central FRSC associated with magmas captured from the volcanic front (Escrig et al., 2012). Despite the proximity of these spreading centers (~30 km), there is a distinct compositional change between them (e.g., Keller et al., 2008). Therefore, these spreading centers are mapped as separate geological assemblages, each consisting of several units (**Fig. 5**).

4.1.1 Mangatolou Triple Junction (MTJ) and Western Rift Zone Assemblages

The MTJ is a ridge-ridge-ridge triple junction with each of the three spreading segments displaying distinct morphologies (**Fig. 5**). The MTJ assemblage consists of a neovolcanic zone along the center of each segment, flanked by older crust that is variably faulted or ridge-like. The western arm (MTJ-W) is oriented ENE, accommodating N-S extension in the basin, and is considered to be a failed rift (Phillips, 2003). This arm has a narrow neovolcanic zone (up to 3 km wide) within a flat axial valley and is heavily faulted, with structures that are oriented ENE to E-W (**Fig. 7d–e**). The southern arm (MTJ-S) consists of two spreading segments that are oriented N-S, with an axial valley containing a neovolcanic zone that is up to 5 km wide. This neovolcanic zone is dominated by sheet flows and small fissures. Distal volcanic ridges along the flanks of the MTJ-S extend up to 40 km to the west of the spreading center and are steeper and have more relief than ridges along the other arms. In the northern part of the MTJ-S arm, the ridges are cross-cut by E-W trending faults associated with the MTJ-W arm. The southern part of the MTJ-S arm is dominated by N-trending structures (**Fig. 7a**) with minor NNW-trending structures in the south (**Fig. 7i**). The northern MTJ arm (MTJ-N) is a single NNE- to NE-trending segment with a broad axial valley up to 18 km wide, which contains the neovolcanic zone and is bounded by steep faults. The northern and southern ends of the segment consist of small volcanic ridges up to ~180 m tall. The central part of the segment has higher relief with a broad shield-like morphology, and a subtle axial graben up to ~2 km wide. Intense off-axis volcanism occurs along a large ridge in the north (centered at 15°18′S, 174°25′W), which is up to 1300 m tall and 17.5 km long, and an area with large, low-relief cratered volcanoes to the NW of the triple junction (centered at 15°30′S, 174°57′W).

To the west of the MTJ-N arm is an area of rifting with inward-dipping faults and no associated neovolcanic zone, which we refer to as the Western Rift assemblage (**Fig. 5**). In the north, the crust is

heavily faulted with overlapping zig-zag structures that that trend NNE, NE, and ENE (**Fig. 7b–d**). In the south, the crust is dominated by younger volcanic flows with morphologies characteristic of sheet flows with collapse features and lesser amounts of pillow flows. Volcanic flows become more common to the west towards the subaerial Niuafo'ou volcanic island, located outside the study area. Cross-cutting the dominant NE-fabric of this area are WNW- and NW-trending volcanic ridges and faults (**Fig. 7g–h**). The area has not been previously described or sampled, and therefore the lithology is unknown.

4.1.2 Northeast Lau Spreading Center (NELSC) Assemblage

The NELSC assemblage follows a NE-oriented spreading center that consists of four segments and displays a gently sigmoidal shape (**Fig. 5**). The northernmost segment is characterized by a 40-km long axial valley resembling a slow-spreading MOR morphology, while the remaining segments in the south are characterized by axial ridges that are ~15 km in length resembling fast-spreading MOR morphologies. The neovolcanic zone is irregular, between 3.4 and 9.7 km wide. The neovolcanic zone of the northernmost segment consists of elongate hummocky lava flows and mounds. There is a gradual progression southward towards a more flat-topped axial volcanic ridge morphology with point-source volcanic cones. Flat-topped volcanic cones occur near the ends of the NELSC. The southernmost segment is the most magmatically-robust, with axial volcanic ridge highs reaching ~1260 m above the surrounding seafloor, with large volcanic cones on each termination of the ridge (Maka and Tafu). Proximal to the neovolcanic zone is older, faulted crust, followed by distal heavily-sedimented ridges. These ridges are symmetrical, indicating a volcanic rather than structural origin. Several large volcanic ridges up to 1570 m tall and 24 km long occur distal to the spreading center, notably to the east of the southern NELSC (centered at 15°24′S, 174°08′W) and to the west of the northern NELSC (centered at 14°55′S, 174°15′W). The structures along this spreading segment are dominantly NNE- and NE-trending (**Fig. 7b–c**), with distal N-trending structures associated with volcanic ridges on the SW and NE sides of the spreading center (**Fig. 7a**).

4.1.3 Fonualei Rift and Spreading Center (FRSC) Assemblage

The FRSC overlaps with the MTJ-S and is oriented N-S to accommodate E-W extension between the Niuafo'ou and Tongan microplates (**Fig. 5**; Sleeper and Martinez, 2016). The FRSC consists of at least six overlapping, left-stepping segments that become progressively closer to the arc towards the south, described by Sleeper et al. (2016). The study area includes the three northern segments, which are ~12–27 km long and are characterized by axial valleys containing a neovolcanic zone up to ~15 km wide. Narrow axial volcanic ridges are surrounded by smooth, featureless seafloor that may be sheet flows or volcaniclastic sediment derived from the nearby volcanic arc. The axial valleys are bounded by steep-sided faults, but unlike other spreading segments in the study area, off-axis faulting is not laterally continuous. The valley flanks are dominated by irregular volcanic ridges and numerous small volcanic cones. To the south of the map area, the axial valleys become less pronounced and there is a transition towards axial ridge morphologies. Based on the width of this assemblage (20–30 km) and the inferred spreading rate (26 mm yr^{-1}; Sleeper and Martinez, 2016) at the northern extent of the FRSC, rifting began between 0.8 and 1.1 Ma. In the north there is an area of robust volcanic activity characterized by coalescing volcanic cones and ridges, as well as a large volcanic ridge, 29-km-long and 1350-m-tall, extending towards the MTJ-N (centered at 15°41′S, 174°38′W). The transition between the FRSC and the MTJ-N is difficult to distinguish. The structures along the FRSC are dominantly N-trending (**Fig. 7a**), with minor NNE- and NNW-trending structures at the northern termination (**Fig. 7b and i**).

This is a provisional file, not the final typeset article

4.1.4 NW Ridge Assemblage

Finally, an enigmatic area consisting of variably oriented volcanic ridges that are not clearly associated with a spreading center occur in the NW part of the map area, referred to here as the NW Ridge Assemblage (**Fig. 5**). Most of the ridges are sub-parallel and oriented NNE to NE (**Fig. 7b–c**), with a major ridge trending and WNW to NNW (**Figs. 7h–i**) rising to a height of 760 m. This major ridge may be an anticline (highlighted in **Fig. 5**). The areas between the ridges is interpreted to be sediment, although backscatter data is lacking in this area and young lava flows may be present. In the north, the ridges are cut by a N-trending rift that extends into the paleo-arc and appears to be heavily sedimented. The southern contact between this unit and the NW Rift assemblage is poorly defined due to a lack of high-resolution multibeam and backscatter data and may be gradational. The lithology of this assemblage is unknown because it has not yet been sampled.

4.2 Lau Rear-Arc Crust

Volcanism that occurs between the active arc front and the spreading centers is referred to as rear-arc volcanism, which is associated with more siliceous lithologies than the back-arc (e.g., Embley and Rubin, 2018). In this region, rear-arc volcanism consists of the Mata volcanoes and the Niuatahi volcano and related features (**Fig. 5**).

4.2.1 Mata Assemblage

The Mata volcano assemblage occurs in the NE part of the study and consists of nine elongate en echelon volcanic ridges composed of boninitic pyroclastic material and lava flows, surrounded by lava flows (**Fig. 5**; Resing et al., 2011a; Rubin and Embley, 2012). These volcanoes have been actively erupting over the last 2 Ma, with older occurrences extending into the fore-arc region (Falloon et al., 2008; Rubin and Embley, 2016; Chadwick et al., 2019). The southern volcanoes, West and East Mata, are 1400–1700 m tall and are elongate along an ENE-trend (**Fig. 7d**). The West Mata volcano is one of only two places in the world where deep-sea submarine eruptions have been witnessed (Resing et al., 2011b). The Mata volcanoes to the north (Taha, Ua, Tolu, Fa, Nima, Ono, Fitu) are smaller (900–1300 m tall) and are variably elongate in ENE- and E-directions.

4.2.2 Niuatahi Assemblage

South of the Mata volcanoes is the Niuatahi assemblage, characterized by the 15-km wide Niuatahi dacite volcano (formerly “Volcano O”), that rises ~1340 m above the surrounding seafloor with a 9-km-wide nested caldera (**Fig. 5**). This volcano is cross-cut by a regional N-trending structure (**Fig. 7a**), with E-W extension indicated by short gaps in the caldera walls in the north and south (Baker et al., 2019). Along this regional structure in the south-central part of the caldera is a 465-m-tall resurgent volcanic cone called Motutahi, which is associated with dacite flows (Park et al., 2015) and active venting (Kim et al., 2009). Niuatahi is surrounded by dacite lava flows that extend ~60 km north and northeastward over an area of ~640 km^2, described by Embley and Rubin (2018). Backscatter signatures indicate at least two ages of flows, with the most recent flows displaying a very high backscatter signal. The chemistry of the flows varies according to location, which Embley and Rubin (2018) use to define three distinct flows, indicating that the eruptions originate from a fissure rather than simply from the Niuatahi volcano. At the map scale here, we group the young flows as a single unit. Lower-than-expected viscosities of these Si-rich lavas are attributed to high magmatic water contents, CO2 contents, and/or high eruptive temperatures (Embley and Rubin, 2018). These dacite flows surround irregularly shaped topographic features, which we interpret to be older constructional volcanic features that represent a central fissure system.

4.3 Tofua Arc Crust

In the study area, the active Tofua arc trends ~18–23° in the south and ~5–8° in the north (**Fig. 5**). The Tofua arc assemblage consists of four units: large arc volcanos (including Volcano L, Volcano K, Niuatoputapu, Tafahi, Curacoa, and other unnamed volcanoes), the Niua volcanic complex, smaller volcanic edifices, and lava flows. The northern portion of the arc has not been sampled extensively; however, samples collected during the SO-263 cruise ranged from trachyandesite to basalt (Haase et al., 2018). This is consistent with sampling along the arc segment adjacent to the FRSC, which is dominantly basaltic andesite (Keller et al., 2008; Sleeper, 2017). The Tofua arc volcanoes are dominantly submarine stratovolcanoes that decrease in size northwards towards the termination of the arc. Many of these volcanoes have large interior caldera structures. Submarine volcanoes K and L, and subaerial volcano Niuatoputapu are all apparently inactive. No historical eruptions have been reported at subaerial Tafahi volcano, but the youthful morphology suggests recent (Holocene) activity (Taylor and Ewart, 1997). A recent eruption at the submarine Curacoa volcano was reported in December 1979 (Global Volcanism Program, 2013). At the northern termination of the arc, the submarine Niua volcanic complex (formerly "Volcano P") has a distinct morphology consisting of numerous overlapping cones and a strongly tectonized appearance. This large complex appears roughly rectangular in plan view, up to 25 km long and 13 km wide, and rises to depths of ~2000 m above the surrounding seafloor. Small (≤100 m tall), dome-like topographic features that are irregularly distributed at the top of the Niua complex are interpreted to be small volcanic edifices. Profuse venting of S-rich magmatic fluids at the Niua North vent site indicate that it is volcanically active (Rubin et al., 2018; Haase et al., 2018). Niua is the only place along the Tofua arc in the map area that has confirmed hydrothermal venting (Niua South vent field; Arculus et al., 2004). Surrounding the northernmost arc volcanoes are young lava flows that are identified by high backscatter signatures. We interpret these flows to be genetically related to the Tofua arc volcanoes based on proximity; however, these flows have not been sampled so this relationship is unconfirmed.

4.4 Vitiaz Paleo-Arc Crust

The Vitiaz paleo-arc crust occurs in the northernmost part of the map area along the STEP boundary and is characterized by a bulging morphology that is heavily tectonized (**Fig. 5**). This forms the Paleo-Arc assemblage, which includes the paleo-fore-arc as the morphology does not allow easy distinction. Few samples from this area have been collected, mainly consisting of adakite and boninite (Falloon et al., 2008; Price et al., 2016). The youngest unit in this assemblage consists of youthful-looking volcanic cones and ridges, forming in areas adjacent to active back-arc volcanism. This area may be capturing magmatism from the back-arc. Backscatter data in these areas is lacking and samples have not been collected. The dominant unit in this assemblage consists of faulted old paleo-arc crust, which contains a high density of structures and includes structures of every orientation (**Fig. 7**). Finally, an area of intensely faulted terrane to the west of the Mata volcanoes is interpreted to be a unit of detached paleo-arc crust. The structural fabric of this block is dominated by WNW-, NW- and NNW-trending fabrics, similar to the paleo-arc crust on the opposite side of the NELSC (**Figs. 7g–i**), and distinct from adjacent assemblages. However, these structural orientations may have been modified during opening of the NELSC, and so the origin remains uncertain. This displaced unit does not show evidence of recent volcanism.

4.5 Clastic Cover Assemblage

Clastic sediments are ubiquitous throughout the basin (**Fig. 5**), forming a cover sequence on top of the basement crust. This assemblage is divided into two units based on morphology: a rippled

This is a provisional file, not the final typeset article

volcaniclastic sediment apron that extends from the volcanic arc, and a smooth featureless plain that is likely a combination of pelagic and volcaniclastic sediment. The contact between these two units is gradational, and the contacts with other units tends to be sharp and can be distinguished by the very low backscatter signature. These units onlap other volcanic units in the map area and are therefore interpreted to be the youngest assemblage in the area.

4.6 Structural Features

A total of 5,892 major normal fault segments (>100 m throw), 12,071 minor normal fault segments (< 100 m throw), 7,420 volcanic ridge segments, and 10,624 lineament segments were interpreted and digitized from the hydroacoustic data (**Fig. 6**). The distribution of structures according to orientation is shown in **Figure 7** (larger maps are available in the Supplementary Material: **Figs. S4** to **S12**), with dominant orientations trending N (0–10°; n = 2959) and NE (30–40°; n = 3033).

Cross-cutting relationships between the structures is evident in areas where there is a measurable offset of one structure (i.e., it is cut by another structure). Cross-cutting relationships are most pronounced in highly tectonized areas, namely, the W Rift zone and the Paleo-Arc crust (**Fig. 7**). Cross-cutting relationships between structures with similar orientations (e.g., N- and NNE-trending) were not observed, instead these features tend to form zig-zag faults. In general, the structures that are the oldest are NNW-, NW-, and WNW-trending, as they are cross-cut by structures of many orientations (including N-, NNE-, NE-, and E- trending structures) and in turn do not cross-cut any structures. The youngest structures are N-, W-, and ENE-trending and these structures are cross-cut only by themselves. A summary of relative cross-cutting relationships of the major structures in the map area is outlined in Table 1. In addition, the direction of the offset provides information about the shear sense for each structure, with R-lateral offsets of the NNE- and N-trending structures, and L-lateral offsets of the E-, ENE-, and W-trending structures (**Table 1**).

4.6.1 Escarpments

There is a distinct three-tiered down-dropped basin topography across the NE Lau Basin (**Fig. 3**). The borders of these tiers are defined by large escarpments with throws of up to 1500 m, which are some of the most striking features in the basin (**Figs. 5 and 7a**). A large escarpment in the NE map area ("Escarpment A" in **Fig. 5**) forms the wall of the ~NNW-trending basin that hosts the Mata volcanoes and the Niua arc volcano. This escarpment is ~30 km long in the map area and has a maximum throw of 890 m. The dip of this escarpment is variable across its length, averaging 36° to the NNE. One dredge sample from this escarpment was dated at 2.03±0.11 Ma (K-Ar dating; Falloon et al., 2007), although the timing of formation of this escarpment is difficult to constrain due to its association with recent volcanic flows (**Fig. 5**). Another ~62-km-long escarpment with a maximum throw of 1070 m occurs at the southern termination of the NELSC ("Escarpment B" in **Fig. 5**) trending ~ENE towards the arc. The average dip is 24° to the NW. Connected to this escarpment in the south is a ~N trending escarpment ("Escarpment C" in **Fig. 5**) that becomes NNE-trending with increasing latitude. This escarpment extends ~37 km before it is interrupted by the MTJ-N at 15°19′S. It continues on the opposite side for another ~38 km. This part of the escarpment appears to be interrupted by a detachment fault at 15°07′S (mapped as a core complex in **Fig. 5**), characterized by NNW-trending corrugations, although there is a high degree of uncertainty in the identification of this feature. This escarpment appears to comprise multiple stepping faults in places, but in general it has a maximum throw of 1095 m, dipping ~24° to the E and NE. It is intersected by an NNW-trending escarpment ("Escarpment D" in **Fig. 5**) that forms the western boundary of the MTJ-N. This escarpment has a maximum throw of 1085 m, decreasing in size southwards towards normally-faulted terrain of the MTJ. Using a cutoff throw of 500 m to define this escarpment, it has a length of

~23 km, and dips of 22° to the SE. These dip angles are likely an underestimate of the true dips due to erosional processes over time, indicated by mass wasting features at the base of some of the escarpments.

5 Results: Shallow Structures (CMTs) and Fault Kinematics

A total of 174 shallow CMTs (≤25) km occur within the map area. Of these, the focal planes of 125 CMTs are interpreted according to their location and proximity to known structural and tectonic features, classified according to orientation in **Figures 7, 8** and **S4** as "beach balls," colored according to interpreted focal plane orientation. The focal planes of 47 CMTs trend 351–10°, 35 CMTs trend 11–30°, 6 CMTs trend 31–50°, 5 CMTs trend 51–70°, 6 CMTs trend 71–90°, 10 CMTs trend 271–290°, 9 CMTs trend 291–310°, and 7 CMTs trend 331–350°. Fault planes were plotted as stereonets to check for consistency in the groupings (**Supplementary Fig. S3**). The fault plane solutions of the remaining 49 CMTs could not be determined (**Fig. 8**).

Shallow normal earthquakes comprise 10% of the CMTs with known focal plane solutions, but these events are restricted to the FRSC in the south of the map area (n = 8; **Fig. 7a**), as well as the northern tip of the NELSC (n = 4; **Fig. 7b, c**). However, extensional rift-parallel horst-and-graben fault patterns are common across the map area, including within neovolcanic zones and off-axis terrains along the main spreading centers (**Fig. 7a**). Extensional structural fabrics in the NE Lau basin are characterized by two main structural trends. The first trend is parallel to sub-parallel with the NELSC and MTJ-N (NNE- to NE-trending; **Fig. 7b, c**). This trend follows the orientation of the Tofua arc between 15°30′S and 17°35′S (southern part of the map area; **Figs. 2 and 5**). The second trend is parallel to sub-parallel with the MTJ-S and FRSC (N-trending; **Fig. 7a**). This trend follows the orientation of the Tofua arc north of 15°30′S (northern part of the map area; **Figs. 2 and 5**). Subordinate structures are orthogonal to these trends but also display normal faulting and extensional features, including the NE- and ENE-trending large volcanic ridges near the southern NELSC and within the Mata volcanic group **(Figs. 5 and 7c,d**). The lack of normal faults in the CMT data likely indicate that extension in the basin is simply not producing high-magnitude (Mw > 5) earthquakes. This may indicate that crustal accretion is dominated by magmatic extension driven by dike injection rather than tectonic extension driven by brittle faulting (e.g., Buck et al., 2005; Ito and Behn, 2008; Anderson et al., 2017).

The CMT data indicate that strike-slip and oblique-slip faulting is widespread across the study area comprising 90% of the interpreted events. This has been described by earlier authors (Hawkins, 1994; Baxter et al., 2020), but here we provide higher-resolution interpretations of the orientation and shear sense interpreted from these CMTs, supported by data of offset features (described in **Section 3.2**). The main N- and NNE-trending structures (along with minor NNW-trending structures) display a right-lateral shear sense (**Fig. 7a, b, i**), accounting for 73% of shallow strike-slip CMT solutions in the area. The N-trending structures are parallel to the FRSC and the MTJ-S, while the NNE-trending structures are parallel to the NELSC. In contrast, NE-trending structures do not display strike-slip motion; instead, these structures may be associated with pure low-magnitude normal faulting with no oblique motion. Subordinate NE-, ENE-, E-, W-, NNW-trending structures display a left-lateral shear sense (**Fig. 7d–g**), accounting for 27% of the shallow strike-slip CMT solutions. The left-lateral CMTs occur near the STEP boundary (n = 7), likely caused by slip between the northern microplates and the Pacific Plate, and farther to the south along the W Rift, MTJ-W, and northern FRSC (n = 19). Dip-slip faults also occur along the STEP boundary east of the NELSC, trending NE, E, W, and WNW (n = 12; **Fig. 7c, e–g**).

This is a provisional file, not the final typeset article

6 Discussion: Mechanisms of Strike-Slip Faulting

Previous authors have suggested that the strike-slip motion in the NE Lau Basin results from strain induced by the transform motion along the northern STEP boundary and asymmetric slab rollback (e.g., Hawkins, 1994; Baxter et al., 2020). This interpretation is supported by the close association of strike-slip CMTs along the boundary, extending southward to ~16°S where strike-slip CMT solutions terminate abruptly. This model suggests that there is a major, regional-scale sinistral shear zone in the NE Lau Basin with a width of approximately 120 km. Notably, there is no evidence for slip along the inferred southern boundary of the shear zone, which instead is dominated by a diffuse zone of seismicity. This consistent with other edge-driven microplate rotation models (e.g., Schouten, 1993). On land, regional shear zones referred to as "megashears" have been interpreted to be induced by the relative motion between two plates (e.g., Arthaud and Matte, 1977; Neev et al., 1982; Campbell and Anderson, 2003) or in intra-plate settings where pre-existing weaknesses in the basement localize shearing (e.g., Frisicale et al., 2010). In these strike-slip fault systems, the fracture patterns typically follow specific geometries referred to as a Riedel shear zone, which can occur at different scales.

Here, we relate the distribution and orientation of right-lateral and left-lateral strike-slip faults within the rigid block boundaries to typical Riedel megashear mechanisms, revealing two distinct sets of structures (**Figs. 9** and **10**). The first set of Riedel megashears are dominated by NNE-trending R′-shears, with minor E-trending R-shears and NNW-trending P-shears (**Fig. 9**) The R'-shears are oriented at a high angle (~75°) counter-clockwise to the boundaries of the megashear zone, which trend ~95° following the orientation of the northern plate boundary. The R'-shears follow the main trends along the NELSC and the W Rift zone and are sub-parallel to MTJ-N. Typically, R′-shears may develop with or after R-shears (e.g., Atmaoui et al., 2006), which are oriented ~10–15° counter-clockwise and synthetic to the megashear zone boundaries. In the study area, R-shears are not widespread, but are sub-parallel to MTJ-W, and closely align with the structural trend of the northern Mata volcanoes and a well-developed strike-slip fault zone in the northwest map area. The P-shears are more difficult to identify but may be manifest as the WNW-trending fabrics in the southern and northern parts of the map area. Within this configuration, compression associated with σ_1 may produce the large anticline associated with the NW Ridge Assemblage and may also result in bulging morphology of the paleo-arc crust. Extension associated with σ_3 is associated with the large ENE-trending volcanic ridges at the southern end of the NELSC, as well as West and East Mata. The orientation of these structures is oblique to the direction of hinge-rollback, suggesting that normal back-arc spreading processes cannot account for all the extension in this area. These extensional features are offset by the R-shears, creating an extensional duplex (**Fig. 9**). North of the FRSC, there appears to be a cluster of NNE-trending seismicity associated with left-lateral fault motion, contrasting the right-lateral motion of faults along other NNE-trending CMTs in the region (**Fig. 9b**). Sleeper (2017) suggests that these strike-slip events are due to a zone of transferred lithosphere, although the regional kinematic control on this reversal is unclear. We therefore interpret the southernmost *diffuse* boundary of the megashear zone to occur near Escarpment B (**Figs. 5** and **9b**).

The second set of Riedel megashears are similar but rotated ~8–12° counter-clockwise relative to the first set of shears (**Fig. 10**). These shears are dominated by N-trending R′-shears, with minor ENE-trending R-shears and W-trending P-shears. The R′-shears follow the orientation of MTJ-S and FRSC, the N-trending fissure system extending north of the Niuatahi volcano, and other N-trending features in the area. The R-shears follow the trend of the West Mata and East Mata volcanoes and the large volcanic ridge to the southwest of Niuatahi, apparently re-activating previous extensional fabric. The megashear zone boundaries trend ~80°, following the previous orientation of R-shears in Model 1 (**Fig. 9b**), and sub-parallel to the orientation of Escarpment B in the south (dashed lines in

Fig. 10). P-shears are also poorly defined for this configuration, but match strike-slip faulting near the northern and southern boundaries of the megashear zone. In this configuration, extension along σ_3 is associated with NE-trending volcanic ridges across the map area, such as the western Mata volcanoes, which are offset by R-shears. This extensional fabric is also parallel to the MTJ-N, the West Rift zone, and the northern and southern terminations of the NELSC and may be enhancing spreading associated with hinge-rollback.

The differing distribution of fault populations from a typical Riedel shear zone (dominated by R-shears) is likely because R′-shears occur at an angle similar to that of faults produced by earlier back-arc extension. It is easier to reactivate these pre-existing faults as opposed to creating new ones as the stress required for frictional sliding along pre-existing faults is much less than the fracture strength (e.g., Byerlee, 1978). Similarly, as the stress-field rotated, pre-existing extensional faults were re-activated as R-shears. This effect has been observed in other back-arc basins (e.g., Manus Basin: Martinez and Taylor, 1996; Morley et al., 2004; Maestro-González et al., 2008). Faults that have undergone strike-slip reactivation tend to have zig-zag geometries with little throw. These morphologies are common throughout the map area but are particularly well-defined in the western part of the map area in the West Rift zone and the MTJ-W arm. Therefore, the observed strike-slip kinematics in the study area support a rigid block model of lithospheric-scale Riedel (mega)shearing, where shearing reactivates pre-existing extensional faults. This indicates that structures in megashear zones may be predisposed to align themselves to the pre-existing fabrics in back-arc settings. Since the tensional stresses in this region are accommodated by re-activation of normal faults as strike-slip faults, other large-scale strike-slip features (such as large-scale drag features) do not manifest in the map view of the area.

The occurrence of two different Riedel megashear geometries in the NE Lau Basin (Models 1 and 2; **Figs. 9b** and **10b**) suggests that the stress field has rotated counterclockwise over time. Structures associated with both geometries are distributed across the map area; however, cross-cutting relationships indicate that Model 1 structures only cross-cut themselves, while Model 2 structures cross-cut both themselves and Model 1 structures (**Table 1**), indicating that the Model 2 structures formed later. In addition, the distribution of modern seismicity revealed by CMTs provides some insight into the timing of Riedel megashear formation. Active seismicity associated with Model 1 megashears occurs mainly in the western portion of the map area (light blue beach balls in **Fig. 9b**), while seismicity associated Model 2 megashears occurs in the central part of the map area closest to the volcanic arc (green and pink beach balls in **Fig. 10b**). Therefore, we propose that Model 1 megashear structures formed first, encompassing the entire map area. This was followed by a change in orientation of the stress field only in the area closest to the arc, forming Model 2 megashear structures. Currently, both configurations remain active in the different regions of the study area.

In general, the geometry and kinematics of the back-arc structures support the idea of a megashear zone, driven by the relative motion between the plates. Additional work is needed to understand the geodynamic controls on the changing stress field, but it is notable that the R'-shears associated with Model 1 are parallel to the orientation of the arc south of 15°30′S (**Fig. 9**), while the R'-shears associated with Model 2 are parallel to the orientation of the arc north of 15°30′S (**Fig. 10**). This suggests that changes in the orientation and magnitude of far-field stresses may have influenced the kinematic regime for back-arc structures and caused segmentation of the volcanic arc, although the nature of the far-field stresses that affected only the eastern part of the NE Lau basin remain enigmatic.

7 Discussion: Links to Microplate Emergence

This is a provisional file, not the final typeset article

Much of our understanding of the emergence of microplates comes from studies in mid-ocean ridge (MOR) settings where plate reorganizations are linked to the propagation of new rifts, forming the boundaries of new microplates (e.g., Wiedicke and Habler, 1993). In contrast, few studies have investigated how these processes operate in back-arc settings where rift propagation is due to subduction-related processes, and the thermal structure of the crust is affected by arc magmatism. Processes such as asymmetric spreading, arc-ward ridge migration, basin-ward arc migration, and the general short-lived nature of spreading centers are common in back-arc basins and less common in MOR settings (e.g., Parson et al., 1990; Martinez and Taylor, 2003).

In the NE Lau Basin, re-orientation of the stress field is associated with a change in the orientation of the extensional axis along a new northward trend. As the extensional axis changes, there is a tendency for rifts to propagate outwards from the tips along the new extensional axis (e.g., CLSC: Parson et al., 1990). This process may be quicker when propagation occurs in thinner crust and where back-arc retreat is the greatest (Parson et al., 1990). This structural reconfiguration may have induced the propagation of new rifts, such as FRSC segments, which are interpreted to be the youngest features in the NE Lau Basin (Schmid et al., 2020). Simultaneous northward propagation of the FRSC and southward propagation of the MTJ-S produce a zone where the spreading centers overlap (**Fig. 5**), and we observe oblique and curved structural patterns that are characteristic of overlapping spreading centers (e.g., North Fiji Basin: Ruellan et al., 1994). Within the map area, major N-trending structures also appear to be extending northward and southward from both tips of the NELSC, associated with V-shaped rift-tip development, and N-trending rifting is occurring along the paleo-arc crust in the northern part of the map area (**Fig. 5**). These structures may reflect the early stages of rift propagation, but higher-resolution magnetic data is needed to investigate the nature of these features.

The re-orientation of the stress field has mainly affected the area closest to the arc, preserving the original megashear zone configuration in the west where it remains seismically active (**Fig. 9b**). This could indicate that the eastern portion of the NE Lau Basin may be in the nascent stages of nanoplate emergence, proposed by Conder and Wiens (2011) as the separate "Niuatoputapu" plate. This is supported by a drastic change in the structural fabric of the basin from west to east across Escarpment C (**Figs. 5–7**). The fabric to the west of this escarpment is dominated by zig-zagging normal-faulted terrane of the West Rift assemblage, and to the east of this escarpment are the N- and NNE-trending volcanic ridges of the NW Ridge and NELSC assemblages. Like other back-arc micro- and nanoplates, the precise boundaries of Niuatoputapu are difficult to define, and may remain only partially separated, as is the case in the southern diffuse boundary of the Niuafo'ou microplate (**Fig. 2**; Sleeper and Martinez, 2016).

8 Discussion: Structural Controls on Off-Axis Magmatic-Hydrothermal Activity

One of the most striking features of the NE Lau Basin is the decentralized nature of volcanism on the seafloor, manifest by large off-axis volcanic ridges, hydrothermally-active rear-arc volcanoes, and widespread lava flows (**Fig. 5**). Previous authors propose that the Mata rear-arc volcanoes are controlled by small crustal tears linked to strike-slip faulting along the STEP boundary (Govers and Wortel, 2005; Embley et al., 2009), but these authors do not provide an explanation for the variable orientations of the Mata volcanoes, along with other enigmatic features such as the siting of the Niuatahi volcano. The structural framework outlined here provides insight into the occurrence of many of these seafloor features. Notably, large off-axis volcanic ridges reflect areas of enhanced magmatism in the map area, and are aligned along several orientations: (1) NE-trending ridges, including the NW NELSC Ridge (**Figs. 5** and **9a**); (2) E-trending ridges forming the northern Mata

volcanoes(**Figs. 5** and **9a**); (3) N-trending ridges, including the N FRSC Ridge and the subtle ridge extending N of Niuatahi (**Figs. 5** and **10a**); (4) NNE-trending ridges, including the West Mata and East Mata volcanoes and the SW Niuatahi Ridge (**Figs. 5** and **10a**). According to our models, the NNE-trending features formed early associated with σ_3 extensional structures in the Model 1 configuration (**Fig. 9b**). These structures were then reactivated as R-shears (Model 2 configuration), along with the formation of the N-trending features during back-arc extension and subsequent re-activation as R′-shears during strike-slip faulting (**Fig. 10b**). In the most recent configuration, extension also occurs along NE-trending structures associated with the new σ_3 orientation. This promotes enhanced magmatism along the southern NELSC and the MTJ-N, as well as rifting along the W Rift zone. We also note that the large Niuatahi rear-arc volcano occurs at the intersection of N-trending and NNE-trending structures. These structures, which have not been previously described, are underlain by linear magnetic anomalies (Austin, 2012), indicating that magma is exploiting these structural pathways. Dacitic sheet flows at surface extend ~60 km northward from Niuatahi, apparently following a N-trending fissure rather than erupting from the volcano itself (Embley and Rubin, 2018). Within the Niuatahi caldera, hydrothermal vents are also aligned along this N-trending regional structure (**Fig. 5**; Haase et al., 2018). Across the map area, hydrothermal vents are closely associated with these regions of enhanced magmatism (**Fig. 5**). Continual re-activation of faults may ensure that these pathways remain permeable despite precipitation of secondary hydrothermal minerals. This complex structural configuration, combined with unusually high upper mantle temperatures and ultrafast subduction rates (e.g., Regelous, 2008), provides the basis for diverse lithologies and eruption styles in the basin, along with a range of style and composition of hydrothermal venting (e.g., Embley and Rubin, 2018; Chadwick et al., 2019).

9 Conclusions

Compared to mid-ocean ridges, back-arc spreading centers are ephemeral features that evolve dynamically in response to oblique convergence, subduction-zone collisions, and microplate interactions. The NE Lau Basin is characterized by extreme tectonic complexity, associated with fast convergence rates, high upper mantle temperatures, and thin oceanic crust (Bevis, et al., 1995; Conder and Wiens, 2006, Embley et al., 2018), producing diverse lithologies and eruption styles in the rear-arc and back-arc regions (e.g., Embley and Rubin, 2018). This complexity is manifest as seafloor fabrics with variably oriented structures. The observed structural patterns reflect the interplay between extension associated with slab-rollback and strike-slip tectonics along the northern STEP boundary, with shallow-crustal strike-slip faulting extending over ~120 km from the STEP boundary. Two distinct sets of structures associated with Riedel shear mechanisms are described for the first time, indicating a recent counter-clockwise rotation of the stress field that primarily affects the region closest to the arc. The structural configurations highlight the importance of re-activation of earlier-formed structures during rotation of the stress-field. The structures that formed and were re-activated in this megashear zone account for the orientations of many of the previously-enigmnatic seafloor features observed, such as the Mata volcanoes and large off-axis volcanic ridges. This study provides important constraints on the geologic and structural evolution of the NE Lau Basin, including the tectonic controls on enhanced magmatism in rear-arc and off-axis regions, as well as the distribution of hydrothermal vent sites in the region.

Supplementary Material

Supplementary material is provided in the electronic appendix associated with this publication.

Data Availability Statement

This is a provisional file, not the final typeset article

The following bathymetric datasets can be found in the Rolling Deck to Repository (R2R): FK171110: https://doi.org/10.7284/907642; KM1024: https://doi.org/10.7284/900840; and KM1129: https://doi.org/10.7284/903993. The SO-263 bathymetric dataset can be found in PANGAEA: https://doi.pangaea.de/10.1594/PANGAEA.892778. The CMT dataset for this study can be found in the Global Centroid-Moment-Tensor database by Dziewonski et al. (1981) and Ekström et al. (2012): www.globalcmt.org.

Conflict of Interest

The authors declare that the research was conducted in the absence of any commercial or financial relationships that could be construed as a potential conflict of interest.

Author Contributions

MOW Prepared all figures, drafted the main text, made equal contributions to the interpretation of the data, and supervised the M.Sc. thesis by CN-J. CN-J completed preliminary data collection, made equal contributions to the interpretation of the data as part of an M.Sc. thesis. KHR secured funding for FK171110 (chief scientist), contributed to bathymetric data collection, interpretation, and editing of the drafts. KH secured funding for SO-263 (chief scientist), contributed to interpretation and editing of drafts. MDH contributed to interpretations and did substantial editing of drafts. ATB contributed to developing methodology for CMT interpretation, interpretation of data, and editing of drafts. MSS Contributed to interpretations and editing of drafts.

Funding

The funding for the project 03G0263 by the German Bundesministerium für Bildung und Forschung is gratefully acknowledged. We acknowledge the support of the Schmidt Ocean Institute for access to the R/V Falkor and ROV SuBastian. MOA acknowledges funding from NSERC-DG and the Connaught New Researcher program (UofT). MOA, MDH, and MSS acknowledge funding from the NSERC-CREATE iMAGE program. This is contribution MERC-ME-2020-003 to the modern-ancient crust project of the Canadian Metal Earth program.

Acknowledgments

We appreciate the efforts of the SO-263 Shipboard Scientific Party, ROV QUEST team, and Captain O. Meyer and his crew on R/V Sonne for their contributions and support. We also thank the FK171110 Shipboard Scientific Party and crew of the R/V Falkor, and the support of the Schmidt Ocean Institute. We gratefully acknowledge S. Merle for processing and compiling the bathymetric data from Rubin et al. (2010), Martinez et al. (2013), and Rubin et al. (2018), and S. Panasiuk for her assistance with bathymetric post-processing using the TTS-shader. We acknowledge L. Calhoun for valuable feedback on the structural interpretations.

References

Anderson, M. O., Hannington, M. D., Haase, K., Schwarz-Schampera, U., Augustin, N., McConachy, T. F., and Allen, K. (2016). Tectonic focusing of voluminous basaltic eruptions in magma-deficient backarc rifts. *Earth and Planetary Science Letters*, 440, 43–55. https://doi.org/10.1016/j.epsl.2016.02.002

651 Anderson, M. O., Chadwick, W. W. Jr., Hannington, M. D., Merle, S. G., Resing, J. A., Baker, E. T.,
652 Butterfield, D. A, Walker, S. L, and Augustin, N. (2017). Geological interpretation of volcanism
653 and segmentation of the Mariana back-arc spreading center between 12.7°N and 18.3°N.
654 *Geochemistry, Geophysics, Geosystems*, 18, 2240–2274. https://doi.org/10.1002/2017GC006813

655 Aruculus, R., and Shipboard Scientific Party (2004). Voyage Summary SS06/2004: Submarine
656 volcanic and hydrothermal activity in the New Hebrides arc-backarc system. *CSIRO Marine*
657 *Research*. Hobart, Australia: CSIRO. Retrieved from
658 http://www.cmar.csiro.au/datacentre/process/data_files/cruise_docs/ss2004_v06_summary.pdf

659 Arthaud, F., and Matte, P. (1977). Late Paleozoic strike-slip faulting in southern Europe and northern
660 Africa: Result of a right-lateral shear zone between the Appalachians and the Urals. *Bulletin of*
661 *the Geological Society of America*, 88, 1305–1320. https://doi.org/10.1130/0016-
662 7606(1977)88<1305:LPSFIS>2.0.CO;2

663 Atmaoui, N., Kukowski, N., Stöckhert, B., and König, D. (2006). Initiation and development of pull-
664 apart basins with Riedel shear mechanism: insights from scaled clay experiments. *International*
665 *Journal of Earth Sicences*, 95, 225–238. https://doi.org/10.1007/s00531-005-0030-1

666 Augustin, N., van der Zwan, F. M., Devey, C. W., Ligi, M., Kwasnitschka, T., Feldens, P., Bantan,
667 R. A., and Basaham, A. S. (2016). Geomorphology of the central Red Sea rift: Determining
668 spreading processes. *Geomorphology*, 274, 162–179.
669 https://doi.org/10.1016/j.geomorph.2016.08.028

670 Austin, R. A. (2012). Early seafloor spreading and variations in crustal accretion in the Lau basin
671 (Doctoral dissertation). Retrieved from ScholarSpace.
672 (https://scholarspace.manoa.hawaii.edu/handle/10125/100916). Honolulu, HI: University of
673 Hawai'i at Manoa.

674 Baker, E. T., Walker, S. L., Massoth, G. J., and Resing, J. A. (2019). The NE Lau Basin: Widespread
675 and abundant hydrothermal venting in the back-arc region behind a superfast subduction zone.
676 *Frontiers in Marine Science*, 6, 382. https://doi.org/10.3389/fmars.2019.00382

677 Baxter, A. T., Hannington, M. D., Stewart, M. S., Emberley, J. M., Breker, K., Krätschell, A.,
678 Petersen, S., Brandl, P. A., Klischies, M., Mensing, R., and Anderson, M. O. (2020). Shallow
679 seismicity and the classification of structures in the Lau back-arc basin. *Geochemistry,*
680 *Geophysics, Geosystems*, 21, e2020GC008924. https://doi.org/10.1029/2020GC008924

681 Beaulieu, S. E., and Szafranski, K. (2019). InterRidge Global Database of Active Submarine
682 Hydrothermal Vent Fields, Version 3.4. Retrieved from http://vents-data.interridge.org.

683 Bevis, M., Taylor, F. W., Schutz, B. E., Recy, J., Isacks, B. L., Helu, S., Singh, R., Kendrick, E.,
684 Stowell, J., Taylor, B., and Calmantli, S. (1995). Geodetic observations of very rapid
685 convergence and back-arc extension at the Tonga arc. *Nature*, 374, 249–251.
686 https://doi.org/10.1038/374249a0

687 Bird, P. (2003). An updated digital model of plate boundaries. *Geochemistry, Geophysics,*
688 *Geosystems*, *4*, 1027. https://doi.org/10.1029/2001GC000252

This is a provisional file, not the final typeset article

689 Brown, L. (2014, April 25). *Texture Shading: A new technique for depicting terrain relief*. Paper
690 presented at the 15h ICA Mountain Cartography Workshop, Banff, Canada. Presentation retrieved
691 from https://app.box.com/v/textureshading

692 Buck, W. R., Lavier, L. L., and Poliakov, A. N. B. (2005). Modes of faulting at mid-ocean ridges.
693 *Nature*, 434, 719–723. https://doi.org/10.1038/nature03358

694 Byerlee, J. D. (1978). Friction of rocks. *Pure and Applied Geophysics*, *116*, 615–626.
695 https://doi.org/10.1007/BF00876528

696 Campbell, P. A., and Anderson, T. H. (2003). Structure and kinematics along a segment of the
697 Mojave-Sonora megashear: A strike-slip fault that truncates the Jurassic continental magmatic arc
698 of southwestern North America. *Tectonics*, 22, 1077. https://doi.org/10.1029/2002TC001367

699 Chadwick, W. W. Jr., Rubin, K. H., Merle, S. G., Bobbitt, A. M., Kwasnitschka, T., and Embley, R.
700 W. (2019). Recent eruptions between 2012–2018 discovered at West Mata submarine volcano
701 (NE Lau Basin, SW Pacific) and characterized by new ship, AUV, and ROV data. *Frontiers in*
702 *Marine Science*, 6, 495. https://doi.org/10.3389/fmars.2019.00495

703 Chase, C. G. (1978). Extension behind island arcs and motions relative to hot spots. *Journal of*
704 *Geophysical Research: Solid Earth*, 83(B11), 5385–5387.
705 https://doi.org/10.1029/JB083iB11p05385

706 Conder, J. A., and Wiens, D. A. (2011). Shallow seismicity and tectonics of the central and northern
707 Lau Basin. *Earth and Planetary Science Letters*, 304, 538–546.
708 https://doi.org/10.1016/j.epsl.2011.02.032

709 Dziewonski, A. M., Chou, T. -A., and Woodhouse, J. H. (1981). Determination of earthquake source
710 parameters from waveform data for studies of global and regional seismicity. *Journal of*
711 *Geophysical Research: Solid Earth*, 86(B4), 2825–2852.
712 https://doi.org/10.1029/JB086iB04p02825

713 Ekström, G., Nettles, M., and Dziewoński, A. M. (2012). The global CMT project 2004–2010:
714 Centroid-moment tensors for 13,017 earthquakes. *Physics of the Earth and Planetary Interiors*,
715 200–201, 1–9. https://doi.org/10.1016/j.pepi.2012.04.002

716 Embley, R. W., Merle, S. G., Lupton, J. E., Resing, J., Baker, E. T., Lilley, M. D., Arculus, R. J., and
717 Crowhurst, P. V. (2009). *Extensive and Diverse Sumbarine Volcanism and Hydrothermal Activity*
718 *in the NE Lau Basin*. Paper presented at the American Geophysical Union Fall Meeting 2009,
719 San Francisco, CA. Abstract retrieved from
720 https://ui.adsabs.harvard.edu/abs/2009AGUFM.V51D1719E/abstract

721 Embley, R. W., and Rubin, K. H. (2018). Extensive young silicic volcanism produces large deep
722 submarine lava flows in the NE Lau Basin. *Bulletin of Volcanology*, 80, 36.
723 https://doi.org/10.1007/s00445-018-1211-7

724 Escrig, S., Bézos, A., Langmuir, C. H., Michael, P. J., and Arculus, R. (2012). Characterizing the
725 effect of mantle source, subduction input and melting in the Fonualei Spreading Center, Lau
726 Basin: Constraints on the origin of the boninitic signature of the back-arc lavas. *Geochemistry,*
727 *Geophysics, Geosystems*, 13, Q10008. https://doi.org/10.1029/2012GC004130.

728 Falloon, T. J., Malahoff, A., Zonenshaina, L. P., and Bogdanova, Y. (1992). Petrology and
729 geochemistry of back-arc basin basalts from Lau Basin spreading ridges at 15°, 18° and 19°S.
730 *Mineralogy and Petrology*, 47, 1–35. https://doi.org/10.1007/BF01165295

731 Falloon, T. J., Danyushevsky, L. V., Crawford, T. J., Maas, R., Woodhead, J. D., Eggins, S. M.,
732 Bloomer, S. H., Wright, D. J., Zlobin, S. K., and Stacey, A. R. (2007). Multiple mantle plume
733 components involved in the petrogenesis of subduction-related lavas from the northern
734 termination of the Tonga arc and northern Lau Basin: Evidence from the geochemistry of arc and
735 backarc submarine volcanics. *Geochemistry, Geophysics, Geosystems*, 8, Q09003.
736 https://doi.org/10.1029/2007GC001619

737 Frisicale, M. C., Dimieri, L. V., Araujo, V. S., Dristras, J. A. (2010) Deformation mechanisms in the
738 mylonite/striped gneiss and mylonite/ultramylonite transition in Sierras de Azul, Rio de la Plata
739 Craton, Buenos Aires. *Revista de la Asociacion Geologica Argentina*, 67, 4–18.

740 GEBCO Compilation Group (2019). GEBCO 2019 Grid [dataset]. doi:10.5285/836f016a-33be-6ddc-
741 e053-6c86abc0788e

742 Global Volcanism Program (2013). Volcanoes of the World, v. 4.8.6. Venzke, E (ed.). Smithsonian
743 Institution. Retrieved from https://doi.org/10.5479/si.GVP.VOTW4-2013

744 Govers, R., and Wortel, M. (2005). Lithosphere tearing at step faults: Response to edges of
745 subduction zones. *Earth and Planetary Science Letters*, 236, 505–523.
746 https://doi.org/10.1016/j.epsl.2005.03.022

747 Haase, K., and Shipboard Scientific Party (2018). SO-263 cruise report Tonga Rift. *Wochenberichte*
748 *und short cruise reports*. Hamburg, Germany: Universität Hamburg. Retrieved from
749 https://www.ldf.uni-hamburg.de/sonne/wochenberichte/wochenberichte-sonne/so263-265/so263-
750 scr.pdf

751 Hall, R. (2002). Cenozoic geological and plate tectonic evolution of SE Asia and the SE Pacific:
752 computer-based reconstructions, model and animations. *Journal of Asian Earth Science*, 20, 353–
753 431. https://doi.org/10.1016/S1367-9120(01)00069-4

754 Hawkins, J. W. (1995). The geology of the Lau Basin. In B. Taylor (Ed.), *Backarc Basins: Tectonics*
755 *and Magmatism* (pp. 63–138). New York, NY: Plenum Press.

756 Heuret, A., and Lallemand, S. (2005). Plate motions, slab dynamics and back-arc deformation.
757 *Physics of the Earth and Planetary Interiors*, 149, 31–51.
758 https://doi.org/10.1016/j.pepi.2004.08.022

759 Ito, G., and Behn, M. D. (2008). Magmatic and tectonic extension at mid-ocean ridges: 2. Origin of
760 axial morphology. *Geochemistry, Geophysics, Geosystems*, 9, Q09O12.
761 https://doi.org/10.1029/2008GC001970

762 Karig, D. E. (1970). Ridges and basins of the Tonga-Kermadec island arc system. *Journal of*
763 *Geophysical Research*, 75, 239–254. https://doi.org/10.1029/JB075i002p00239

This is a provisional file, not the final typeset article

764 Keller, N. S., Arculus, R. J., Hermann, J., and Richards, S. (2008). Submarine back-arc lava with arc
765 signature: Fonualei Spreading Center, northeast Lau Basin, Tonga. *Journal of Geophysical*
766 *Research: Solid Earth*, 113, B08S07. https://doi.org/10.1029/2007JB005451

767 Kim, J., Son, J. -W., Kim, K. -H., Shim, W. J., Kim, C. H., Lee, K. -Y. (2009). Venting sites along
768 the Fonualei and Northeast Lau Spreading Centers and evidence of hydrothermal activity at an
769 off-axis caldera in the northeastern Lau Basin. *Geochemical Journal*, 43, 1–13.
770 https://doi.org/10.2343/geochemj.0.0164

771 Klischies, M., Petersen, S., and Devey, C. W. (2019). Geological mapping of the Menez Gwen
772 segment at 37°50′N on the Mid-Atlantic Ridge: Implications for accretion mechanisms and
773 associated hydrothermal activity at slow-spreading mid ocean ridges. *Marine Geology*, 412, 107–
774 122. https://doi.org/10.1016/j.margeo.2019.03.012

775 Langmuir, C. H., Bézos, A., Escrig, S., and Parman, S. W. (2006). Chemical Systematics and
776 Hydrous Melting of the Mantle in Back-Arc Basins. In D. M. Christie, C. R. Fisher, S. -M. Lee,
777 and Givens, S. (Eds.). *Back-Arc Spreading Systems: Geological, Biological, Chemical, and*
778 *Physical Interactions*, Vol. 166, pp. 87–146. Washington, DC:American Geophysical Union,
779 Geophysical Monograph Series. https://doi.org/10.1029/166GM07

780 Lupton, J., Rubin, K. H., Arculus, R., Lilley, M., Butterfield, D., Resing, J., et al. (2015). Helium
781 isotope, He, and Ba-Nb-Ti signatures in the northern Lau Basin: Distinguishing arc, back-arc, and
782 hotspot affinities: Helium and Carbon in Northern Lau Basin. *Geochemistry, Geophysics,*
783 *Geosystems*, 16, 1133–1155. https://doi.org/10.1002/2014GC005625

784 Maestro-González, A., Bárcenas, P., Vázquez, J. T., and Díaz-del-Río, V. (2008). The role of
785 basement inheritance faults in the recent fracture system of the inner shelf around Alboran Island,
786 Western Mediterranean. *Geo-Marine Letters*, 28, 53–64. https://doi.org/10.1007/s00367-007-
787 0089-8

788 Martinez, F., and Taylor, B. (1996). Backarc spreading, rifting, and microplate rotation, between
789 transform faults in the Manus Basin. *Marine Geophysical Researches*, 18, 203–224.
790 https://doi.org/10.1007/BF00286078

791 Martinez, F., and Taylor, B. (2003). Controls on back-arc crustal accretion: Insights from the Lau,
792 Manus and Mariana basins. In R. D. Larter and P. T. Leat (Eds.). *Intra-Oceanic Subduction*
793 *Systems: Tectonic and Magmatic Processes* (Vol. 219, pp. 19–54). London, UK: The Geological
794 Society of London, Special Publications. https://doi.org/10.1144/GSL.SP.2003.219.01.02

795 Martinez, F., and Shipboard Scientific Party (2013). R/V Kilo Moana KM1129 [cruise data].
796 Available from *Rolling Deck to Repository (R2R)*: https://doi.org/ 10.7284/903698

797 McKenzie, D. P. (1969). The relation between fault plane solutions for earthquakes and the directions
798 of the principal stresses. *Bulletin of the Seismological Society of America*, 59, 591–601.

799 Morley, C. K., Haranya, C., Phoosongsee, W., Pongwapee, S., Kornsawan, A., and Wonganan, N.
800 (2004). Activation of rift oblique and rift parallel pre-existing fabrics during extension and their
801 effect on deformation style: examples from the rifts of Thailand. *Journal of Structural Geology*,
802 26, 1803–1829. https://doi.org/10.1016/j.jsg.2004.02.014

Neev, D., Hall, J. K., and Saul, J. M. (1982) The Pelusium megashear system across Africa and associated lineament swarms. *Journal of Geophysical Research*, 87, 1015–1030. https://doi.org/10.1029/JB087iB02p01015

Neves, M., Searle, R., and Bott, M. (2003). Easter microplate dynamics. *Journal of Geophysical Research: Solid Earth*, 108, 2213. https://doi.org/10.1029/2001JB000908

Nijholt, N., and Govers, R. (2015). The role of passive margins on the evolution of subduction-transform edge propagators (STEPs). *Journal of Geophysical Research: Solid Earth*, 120, 7203–7230. https://doi.org/10.1002/2015JB012202

Nilsson, K., Florendo, F., and Hawkins, J. W. (1989). Petrology of a nascent triple junction, northeastern Lau Basin. *Eos*, 73, 1389.

Park, J. -W., Campbell, I. H., Kim, J., Moon, J. -W. (2015). The role of late sulfide saturation in the formation of a Cu- and Au-rich magma: Insights from the platinum group element geochemistry of Niuatahi-Motutahi lavas, Tonga rear arc. *Journal of Petrology*, 56, 59–81. https://doi.org/10.1093/petrology/egu071

Parson, L., Pearce, J. A., Murton, B., and Hodkinson, R. (1990). Role of ridge jumps and ridge propagation in the tectonic evolution of the Lau back-arc basin, southwest Pacific. *Geology*, 18, 470–473. https://doi.org/10.1130/0091-7613(1990)018<0470:RORJAR>2.3.CO;2

Pelletier, B., Lagabrielle, Y., Benoit, M., Cabioch, G., Calmant, S., and Garel, E. (2001). Newly identified segments of the Pacific-Australia plate boundary along the North Fiji transform zone. *Earth and Planetary Science Letters*, 193, 347–358. https://doi.org/10.1016/S0012-821X(01)00522-2

Phillips, D. A. (2003). Crustal motion studies in the Southwest Pacific: Geodetic measurements of plate convergence in Tonga, Vanuatu and the Solomon Islands (Doctoral dissertation). Retrieved from ProQuest. (https://search.proquest.com/docview/305327521). Honolulu, HI: University of Hawai'i at Manoa.

Price, A. A., Jackson, M. G., Blichert-Toft, J., Blusztajn, J., Conaster, C. S., Konter, J. G., Koppers, A. A. P., and Kurz, M. D. (2016). Geochemical evidence in the northeast Lau Basin for subduction of the Cook-Austral volcanic chain in the Tonga Trench. *Geochemistry, Geophysics, Geosystems*, 17, 1694–1724. https://doi.org/10.1002/2015GC006237

Regelous, M., Turner, S., Falloon, T. J., Taylor, P., Gamble, J., and Green, T. (2008). Mantle dynamics and melting beneath Niuafo'ou Island and the northern Lau back-arc basin. *Contributions to Mineralogy and Petrology*, 156, 103–118. https://doi.org/10.1007/s00410-007-0276-7

Resing, J., and Shipboard Scientific Party (2009). R/V Thomas G. Thompson TN234 [cruise data]. Available from *Rolling Deck to Repository (R2R)*: https://doi.org/10.7284/903993

Resing, J. A., Baker, E. T., Luption, J. E., Lilley, M. D., Rubin, K. H., and Buck, N. J. (2011a, December 5–9). *The Chemistry of Hydrothermal venting at a Volcano "O", a large Submarine Volcano in the NE Lau Basin*. Paper presented at the American Geophysical Union Fall Meeting

This is a provisional file, not the final typeset article

2011, San Francisco, CA. Abstract retrieved from https://ui.adsabs.harvard.edu/abs/2011AGUFM.V53D2652R/abstract

Resing, J. A., Rubin, K. H., Embley, R. W., Lupton, J. E., Baker, E. T., Dziak, R. P., Baumberger, T., Lilley, M. D., Huber, J. A., Shank, T. M. et al. (2011b). Active submarine eruption of boninite in the northeastern Lau Basin. *Nature Geoscience*, 4, 799–806. https://doi.org/10.1038/ngeo1275

Rubin, K., and Shipboard Scientific Party (2010). R/V Kilo Moana KM1024 [cruise data]. Available from *Rolling Deck to Repository (R2R)*: https://doi.org/10.7284/900840

Rubin, K., and Embley, R. (2012). *Identification and implications of a submarine monogenetic field in the NE Lau Basin*. Paper presented at the American Geophysical Union Fall Meeting 2012, San Francisco, CA. Abstract retrieved from https://ui.adsabs.harvard.edu/abs/2012AGUFM.V44C..08R/abstract

Rubin, K., Embley, R., Arculus, R., and Lupton, J. (2013). *Magmatically greedy rear-arc volcanoes of the N. Tofua segment of the Tonga arc*. Paper presented at the American Geophysical Union Fall Meeting 2013, San Francisco, CA. Abstract retrieved from https://ui.adsabs.harvard.edu/abs/2013AGUFM.V13I..04R/abstract

Rubin, K. H., and Embley, R. W. (2016). Tectonic and volcanic interplays in earths largest and only known active boninite volcano province. *Geological Society of America Abstracts with Programs*, 48(7). https://doi.org/10.1130/abs/2016AM-286764.

Rubin, K., and Shipboard Scientific Party (2018). R/V Falkor FK171110 [cruise data]. Available from *Rolling Deck to Repository (R2R)*: https://doi.org/10.7284/907642

Ruellan, E., Huchon, P., Auzende, J.-M., Gracia, E. (1994) Propagating rift and overlapping spreading center in the North Fiji Basin. *Marine Geology*, 116, 37–56. https://doi.org/10.1016/0025-3227(94)90167-8

Ruellan, E., Delteil, J., Wright, I., and Matsumoto, T. (2003). From rifting to active spreading in the Lau Basin - Havre trough backarc system (SW Pacific): Locking/unlocking induced by seamount chain subduction. *Geochemistry, Geophysics, Geosystems*, 4, 8909. https://doi.org/10.1029/2001GC000261

Schmid, F., Kopp, H., Schnabel, M., Dannowski, A., Heyde, I., Riedel, M., Hannington, M.D., Engels, M., Beniest, A., Klauke, I., Augustin, N., Brandl, P.A., and Devey, C. (2020). Crustal structure of the Niuafo'ou Microplate and Fonulaei Rift and Spreading Center in the Northeaster Lau Basin, Southwestern Pacific. *Journal of Geophysical Research: Solid Earth*, 125, e2019JB019184. https://doi.org/10.1029/2019JB019184

Scholz, C., and Campos, J. (1995). On the mechanism of seismic decoupling and back arc spreading at subduction zones. *Journal of Geophysical Research: Solid Earth*, 100, 22103–22115. https://doi.org/10.1029/95JB01869

Schouten, H., Klitgord, K. D., and Gallo, D. G. (1993). Edge-driven microplate kinematics. *Journal of Geophysical Research: Solid Earth*, 98, 6689–6701. https://doi.org/10.1029/92JB02749

878 Sdrolias, M., and Muller, R. D. (2006). Controls on back-arc basin formation. *Geochemistry,*
879 *Geophysics, Geosystems*, 7, Q04016. https://doi.org/10.1029/2005GC001090

880 Sleeper, J. D. (2017). Tectonic and Magmatic Controls on Extension and Crustal accretion in
881 Backarc Basins, Insights from the Lau Basin and Southern Mariana Trough (Doctoral
882 dissertation). Retrieved from SOEST.
883 (https://www.soest.hawaii.edu/GG/academics/theses/Sleeper_Dissertation.pdf). Honolulu, HI:
884 University of Hawai'i at Manoa.

885 Sleeper, J. D., and Martinez, F. (2016). Geology and kinematics of the Niuafo'ou microplate in the
886 northern Lau Basin. *Journal of Geophysical Research: Solid Earth*, 121, 4852–4875.
887 https://doi.org/10.1002/2016JB013051

888 Sleeper, J. D., Martinez, F., and Arculus, R. (2016). The Fonualei Rift and Spreading Center: Effects
889 of ultraslow spreading and arc proximity on back-arc crustal accretion. *Journal of Geophysical*
890 *Research: Solid Earth*, 121, 4814–4835. https://doi.org/10.1002/2016JB013050

891 Tappin, D., Bruns, T., and Geist, E. (1994). Rifting of the Tonga/Lau ridge and formation of the Lau
892 backarc basin: Evidence from site 840 on the Tonga Ridge. In J. Hawkins, L. Parson, J. Allan, et
893 al. (Eds.) *Proceedings of the Ocean Drilling Program, Scientific Results* (Vol. 135, pp. 367–371).
894 College Station, TX: Ocean Drilling Program.

895 Taylor, B., Zellmer, K., Martinez, F., and Goodliffe, A. (1996). Sea-floor spreading in the Lau back-
896 arc basin. *Earth and Planetary Science Letters*, 144, 35–40. https://doi.org/10.1016/0012-
897 821X(96)00148-3

898 Taylor, P.W., and Ewart, A. (1997). The Tofua volcanic arc, Tonga, SW Pacific: Review of historic
899 volcanicactivity. Australian Volcanological Investigations (AVI) Occasional Report No. 97/01.
900 Pymble, New South Wales: Australian Volcanological Investigations.

901 Tian, L., Castillo, P. R., Hilton, D. R., Hawkins, J. W., Hanan, B. B., and Pietruszka, A. J. (2011).
902 Major and trace element and Sr-Nd isotope signatures of the northern Lau Basin lavas:
903 Implications for the composition and dynamics of the back-arc basin mantle. *Journal of*
904 *Geophysical Research: Solid Earth*, 116, B11201. https://doi.org/10.1029/2011JB008791

905 Wiedicke, M., and Collier, J. (1993). Morphology of the Valu Fa spreading ridge in the southern Lau
906 basin. *Journal of Geophysical Research: Solid Earth*, 98, 11769–11782.

907 Wiedicke, M., and Habler, W. (1993). Morphotectonic characteristics of a propagating spreading
908 system in the northern Lau Basin. *Journal of Geophysical Research: Solid Earth*, 98, 11,783–
909 11,797. https://doi.org/10.1029/93JB00707

910 Wysoczanski, R., Leonard, G., Gill, J., Wright, I., Calvert, A., McIntosh, W., Jicha, B., Gamble, J.,
911 Timm, C., Handler, M., Drewes-Todd, E., and Zohrab, A. (2019). Ar-Ar age constraints on the
912 timing of Havre Trough opening and magmatism. *New Zealand Journal of Geology and*
913 *Geophysics*, 62, 371–377. https://doi.org/10.1080/00288306.2019.1602059

914 Zellmer, K. E., and Taylor, B. (2001). A three-plate kinematic model for Lau Basin opening.
915 *Geochemistry, Geophysics, Geosystems*, 2, 2000GC000106.
916 https://doi.org/10.1029/2000GC000106

This is a provisional file, not the final typeset article

Zhang, H., Yan, Q., Li, C., Zhu, Z., Zhao, R., and Shi, X. (2018). Geochemistry of diverse lava types from the Lau Basin (SW Pacific): Implications for complex back-arc mantle dynamics. *Geological Journal*, 54, 3643–3659. https://doi.org/10.1002/gj.3354

920 **Figures**

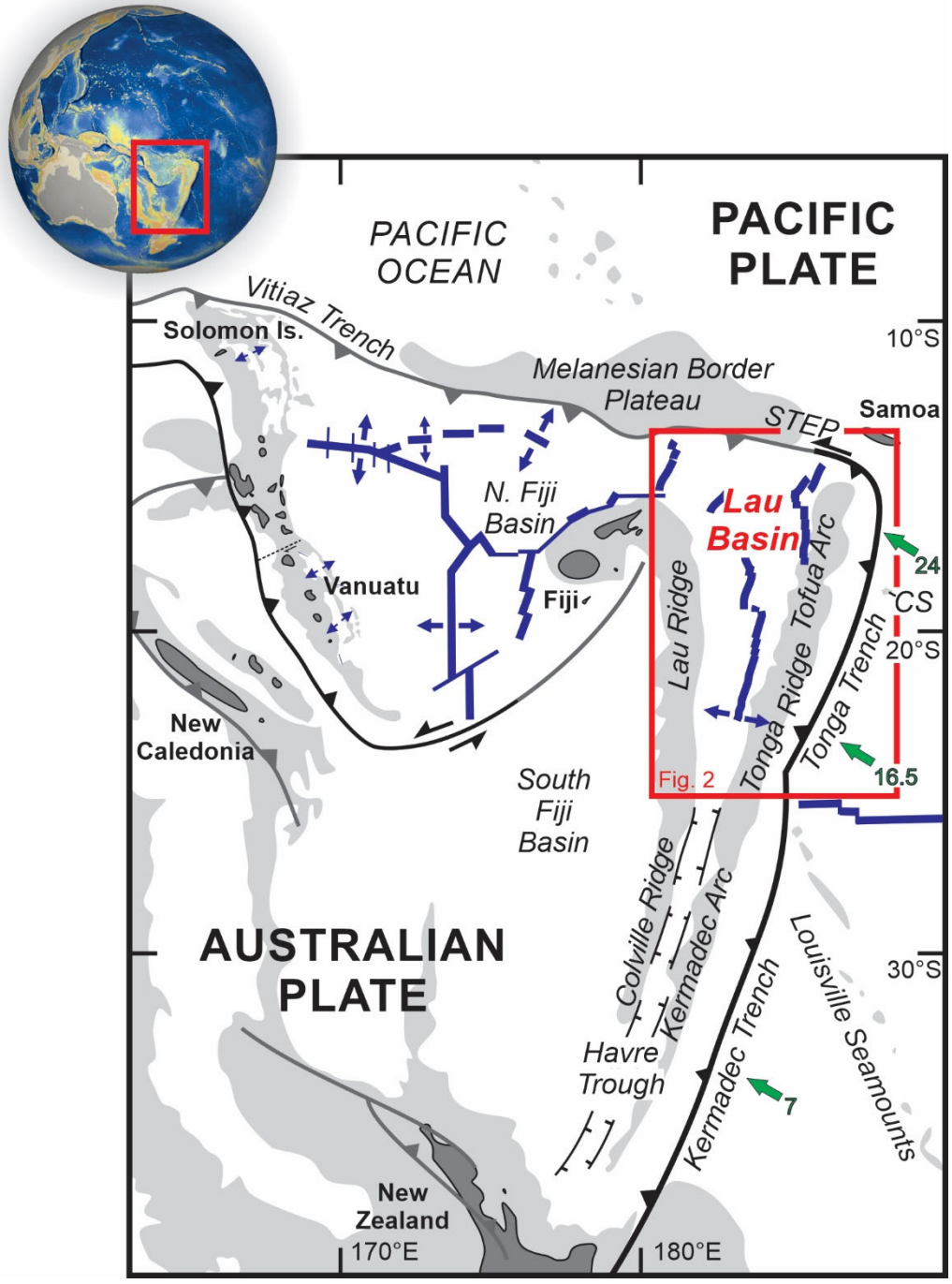

921

922 **Figure 1.** Geographic location and tectonic features of the southwest Pacific modified from Hall
923 (2002). Light grey areas represent the 2000 m isobaths, green arrows indicate convergence directions
924 and rates (cm y^{-1}) from Bevis et al. (1995), and blue lines represent spreading centers. CS = Capricorn
925 Seamount(s), STEP = Subduction-Transform-Edge-Propagator boundary.

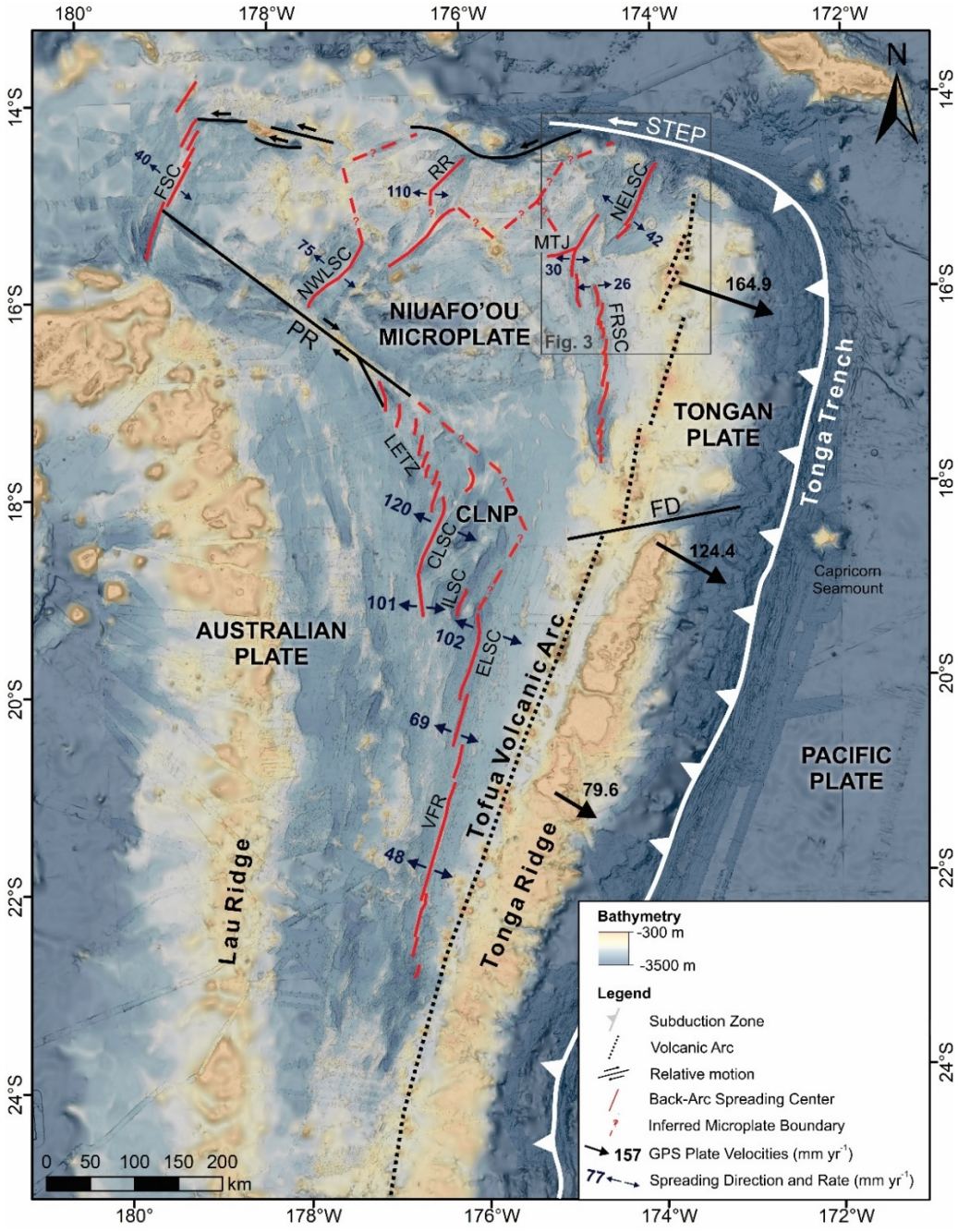

Figure 2. Tectonic features and regional bathymetry of the NE Lau Basin compiled from Rubin et al., 2010, Martinez et al., 2013, Rubin et al., 2018, Haase et al. (2018) and GEBCO compilation group (2019). Inferred microplate boundaries based on seismicity from Conder and Wiens (2011), GPS velocities of Tonga relative to Australia from Phillips (2003) and spreading directions and rates (mm yr^{-1}) for the FSC from Pelletier et al. (2001), for the NWLSC and RR from Lupton et al. (2015) following Bird (2003), and for the CLSC, ELSC, FRSC, LETZ, MTJ, NELSC, and VFR from Sleeper and Martinez (2016). CLNP = Central Lau Nano-Plate; CLSC = Central Lau Spreading Center; ELSC = Eastern Lau Spreading Center; FD = Fonualei Discontinuity; FRSC = Fonualei Rift and Spreading Center; FSC = Futuna Spreading Center; ILSC = Intermediate Lau Spreading Center; LETZ = Lau Extensional Transform Zone; MTJ = Mangatolu Triple Junction; NELSC = North-East Lau Spreading Center; NWSC = North-West Lau Spreading Center; PR = Peggy Ridge; RR = Rochambeau Rifts; VFR = Valu Fa Ridge.

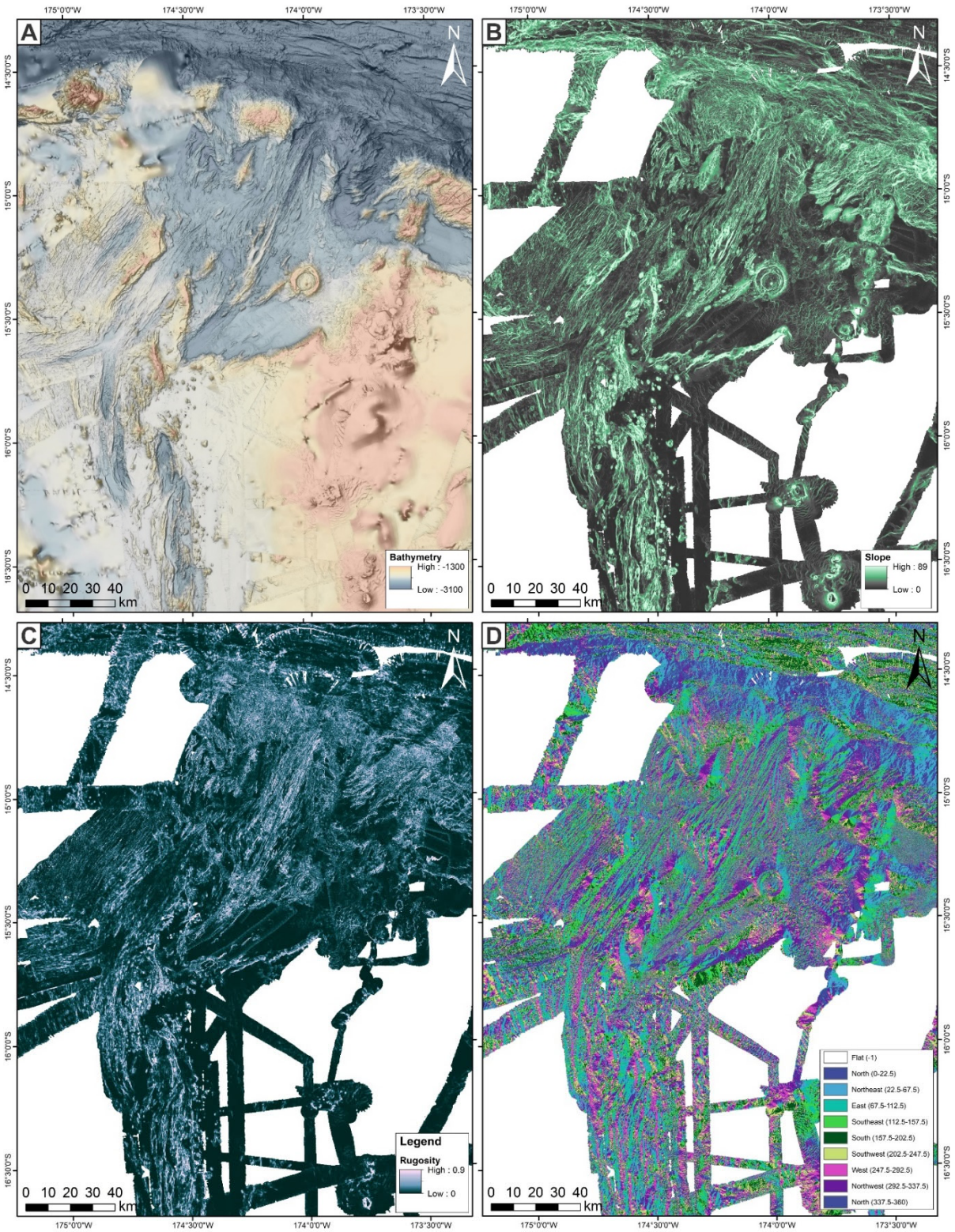

Figure 3. Ship multibeam bathymetry and derived datasets from the NE Lau Basin: (a) ship multibeam bathymetry from Rubin et al. (2010), Martinez et al. (2013), Rubin et al. (2018), and Haase et al. (2018), overlain on the GEBCO 2019 regional bathymetric grid (GEBCO compilation group, 2019), processed using Terrain Texture Shading (after Brown, 2014); (b) slope of the ship multibeam bathymetry compilation; (c) rugosity (or vector ruggedness measure) of the ship multibeam bathymetry compilation; and (d) aspect of the ship multibeam bathymetry compilation.

This is a provisional file, not the final typeset article

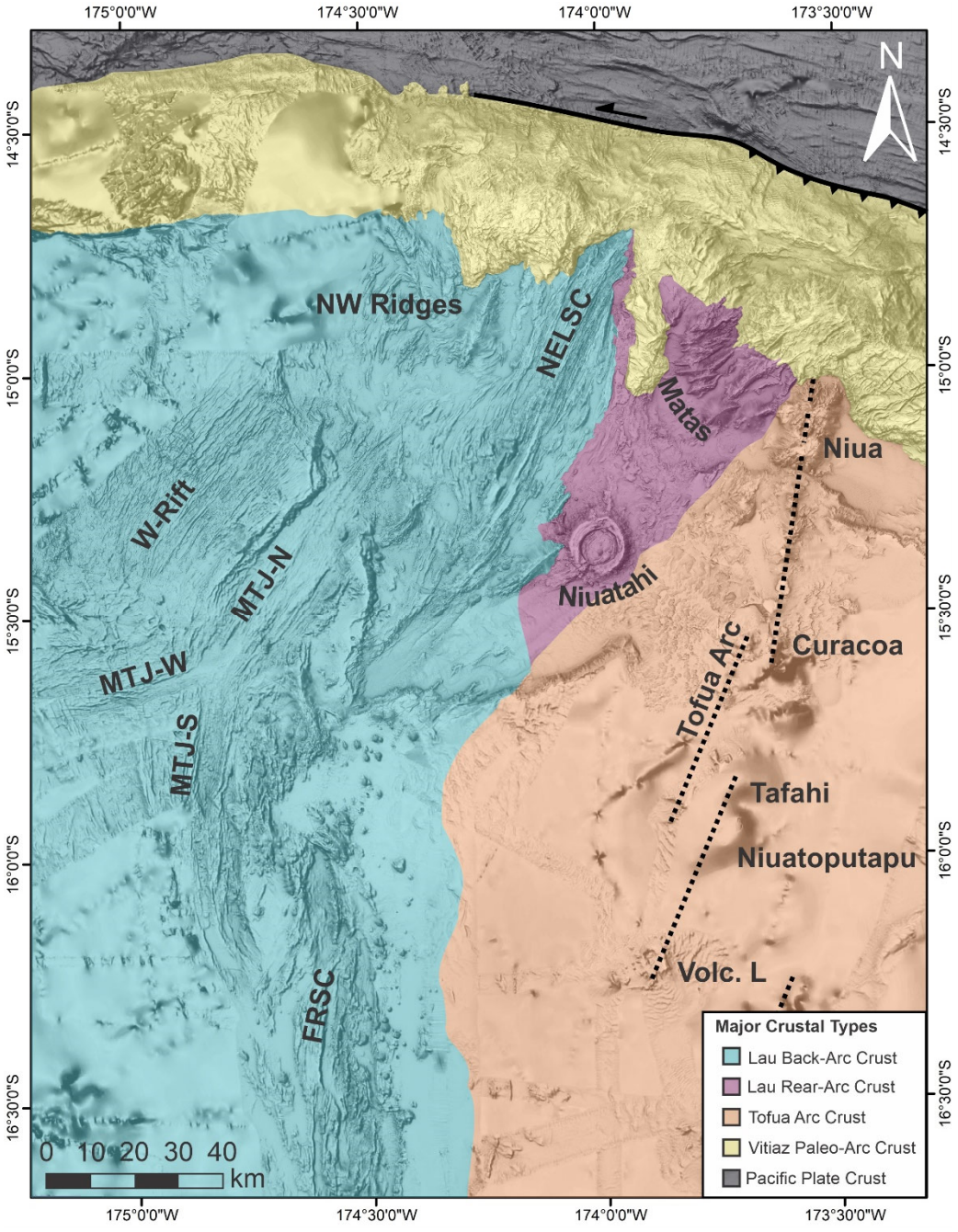

Figure 4. Crustal types in the study area overlain on a compilation of ship multibeam bathymetry (from Rubin et al., 2010; Martinez et al., 2013; Rubin et al., 2018; Haase et al., 2018) and the GEBCO 2019 regional bathymetric grid (GEBCO compilation group, 2019). Abbreviations as in **Figure 2**.

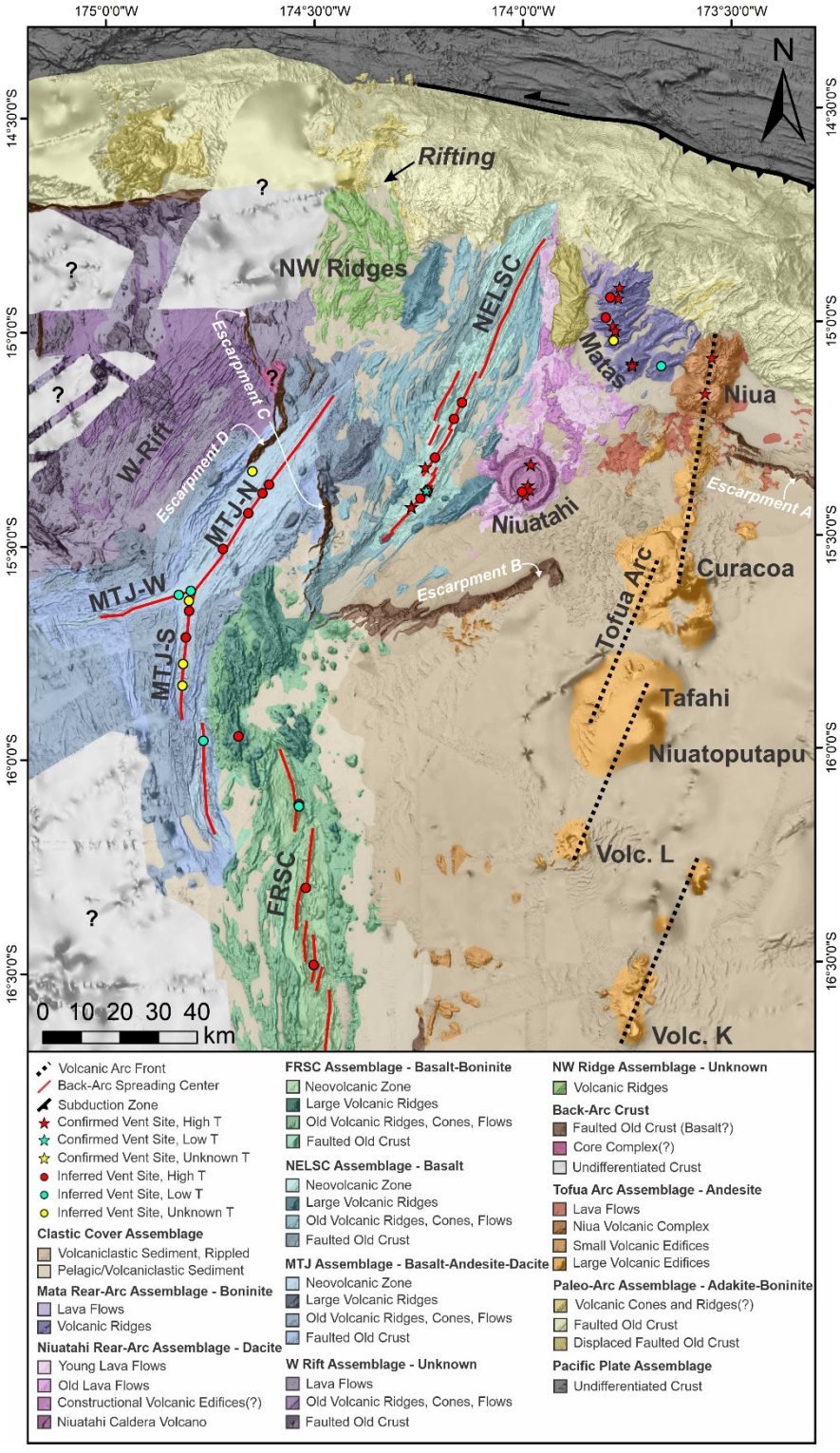

Figure 5. Remote-predicted geological map of the NE Lau basin interpreted from seafloor geomorphology and limited sampling (**Fig. S1**), overlain on a compilation of ship multibeam bathymetry (from Rubin et al., 2010; Martinez et al., 2013; Rubin et al., 2018; Haase et al., 2018) and the GEBCO 2019 regional bathymetric grid (GEBCO compilation group, 2019). Hydrothermal vent sites compiled from the FK171111 and SO-263 cruises (Rubin et al., 2018; Haase et al., 2018), InterRidge Vents Database v. 3.4 (Beaulieu and Szafranski, 2019), and Baker et al. (2019). Abbreviations as in **Figure 2**. Additional details on map units outlined in **Supplementary Table S1**.

This is a provisional file, not the final typeset article

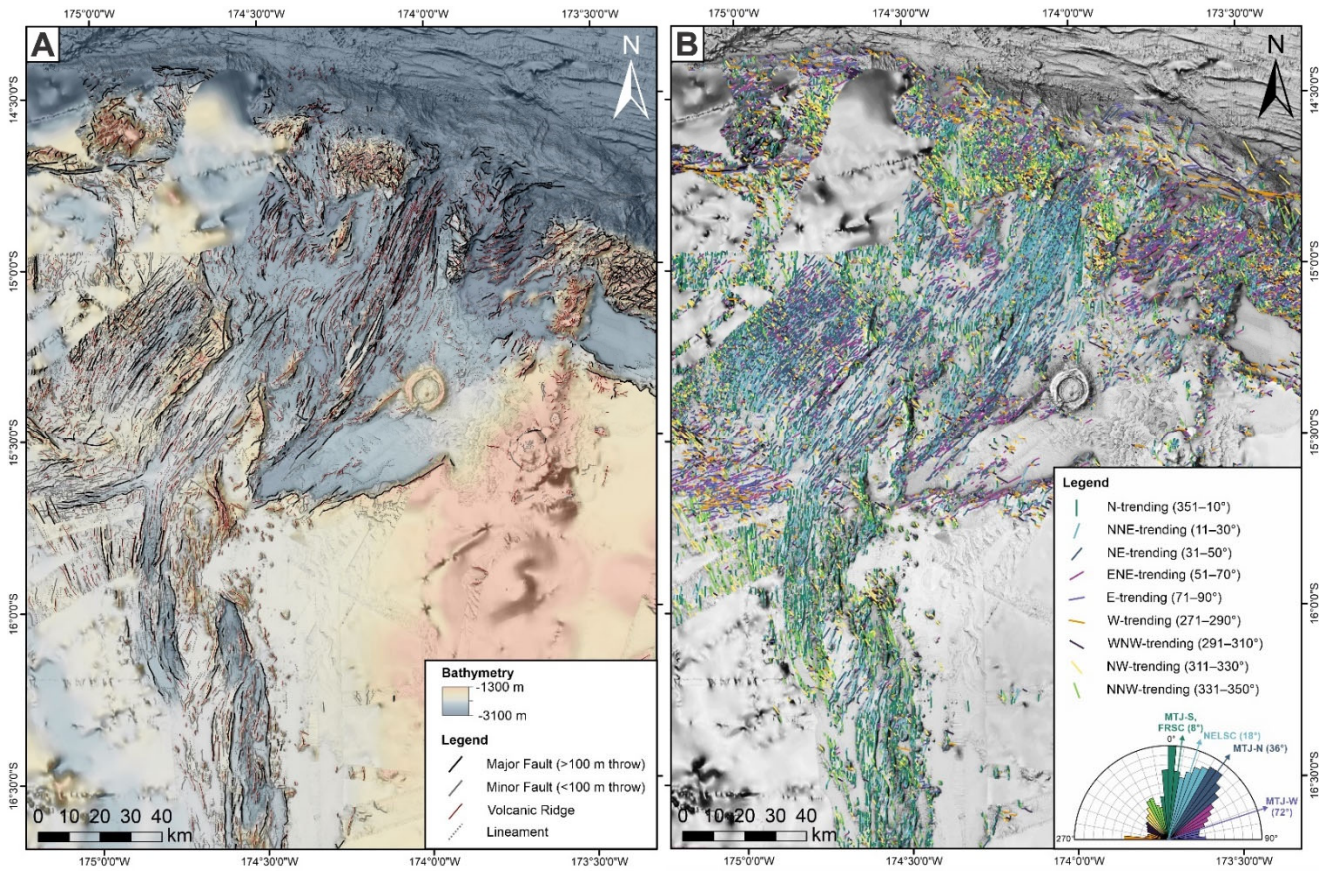

Figure 6. Interpreted structural lineaments in the NE Lau basin overlain on a compilation of ship multibeam bathymetry (from Rubin et al., 2010; Martinez et al., 2013; Rubin et al., 2018; Haase et al., 2018): (a) by type, and (b) by orientation.

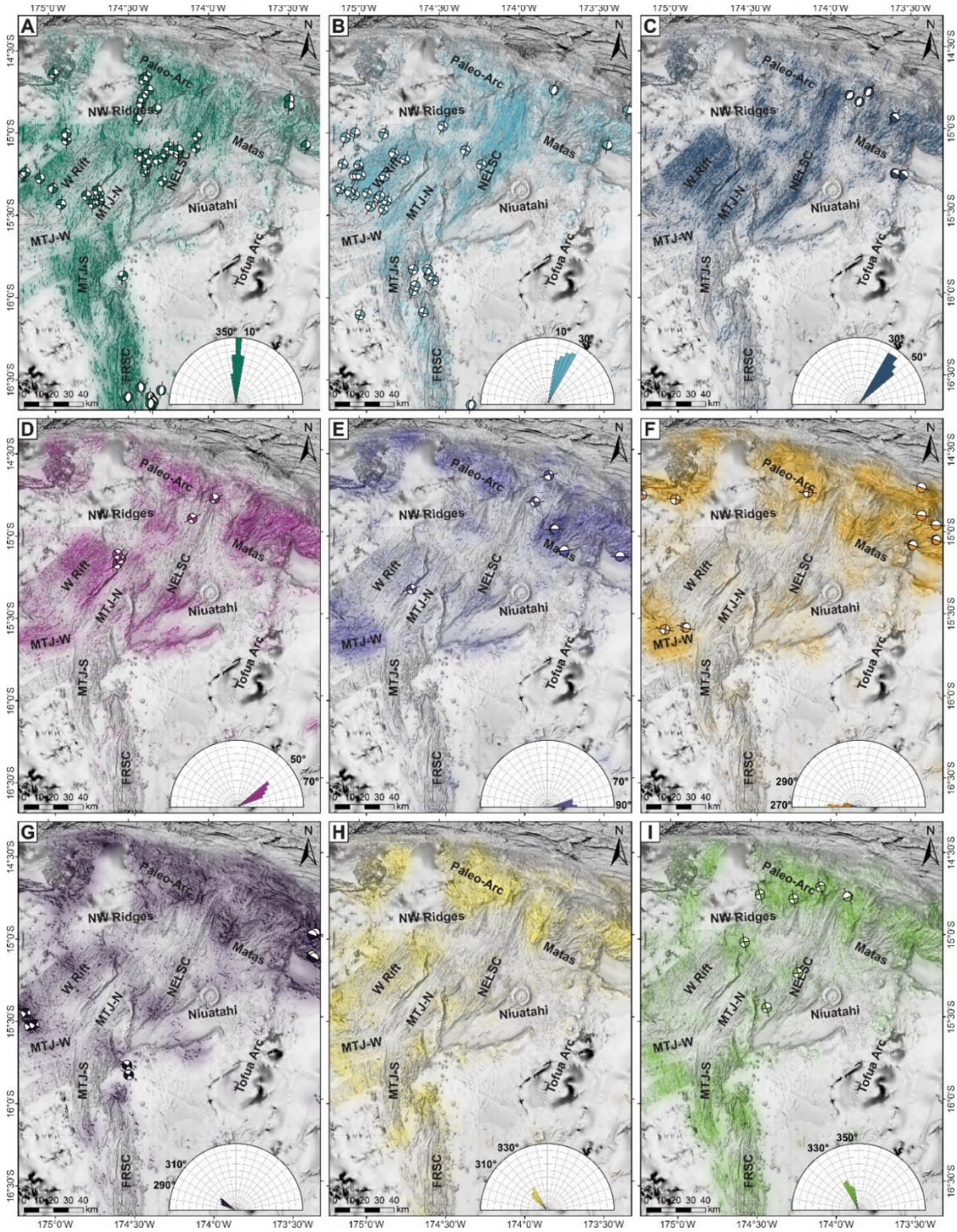

Figure 7. Interpreted structural lineaments, relative lineament densities (lineament km per km^2), and shallow (≤25 km) CMT focal mechanisms from Harvard (www.globalcmt.org; Dziewonski et al., 1981; Ekström et al., 2012), classified according to interpreted focal plane solution: (a) N-trending (max. 0.57 km/km^2), (b) NNE-trending (max. 1.25 km/km^2), (c) NE-trending (max. 1.04 km/km^2), (d) ENE-trending (max. 0.64 km/km^2), (e) E-trending (max. 0.57 km/km^2), (f) W-trending (max. 0.24 km/km^2), (g) WNW-trending (max. 0.29 km/km^2), (h) NW-trending (max. 0.29 km/km^2), (i) NNW-trending (max. 0.33 km/km^2). Stereonets of CMTs grouped according to interpreted focal plane solution shown in **Supplementary Figure S3**, and close-ups of each of the maps is shown in **Supplementary Figures S4** to **S12**. Abbreviations as in **Figure 2**.

This is a provisional file, not the final typeset article

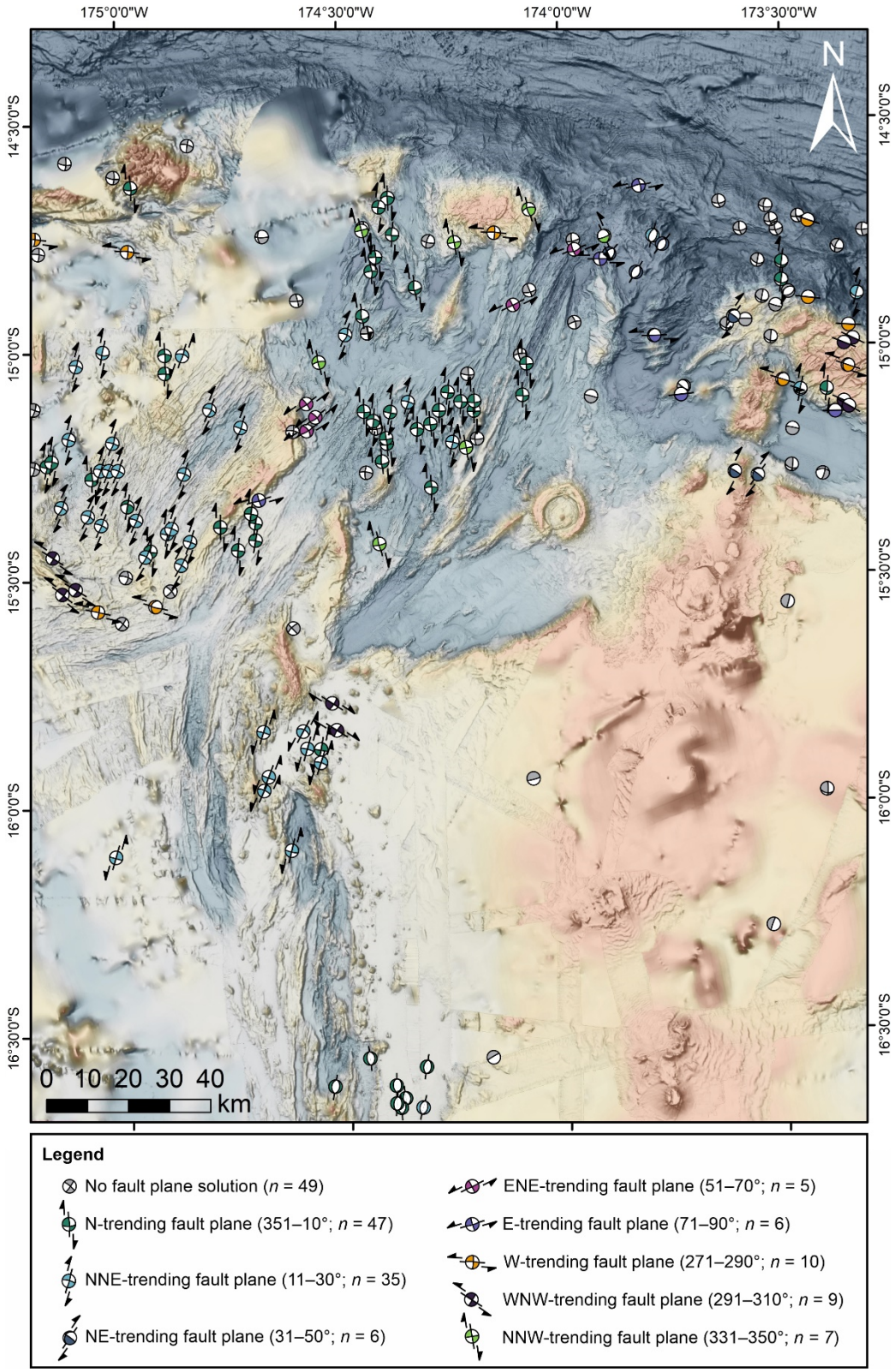

Figure 8. A total of 174 CMTs with shallow depths (≤25 km) occur within the map area (www.globalcmt.org; Dziewonski et al., 1981; Ekström et al., 2012). Of these, 125 CMT focal plane solutions are interpreted by association with the dominant orientation of the seafloor fabric (see **Supplementary Fig. S2**). The colors of the beachball represent the orientation of the focal plane solution outlined in the legend and shown in detail in **Figure 7**.

978

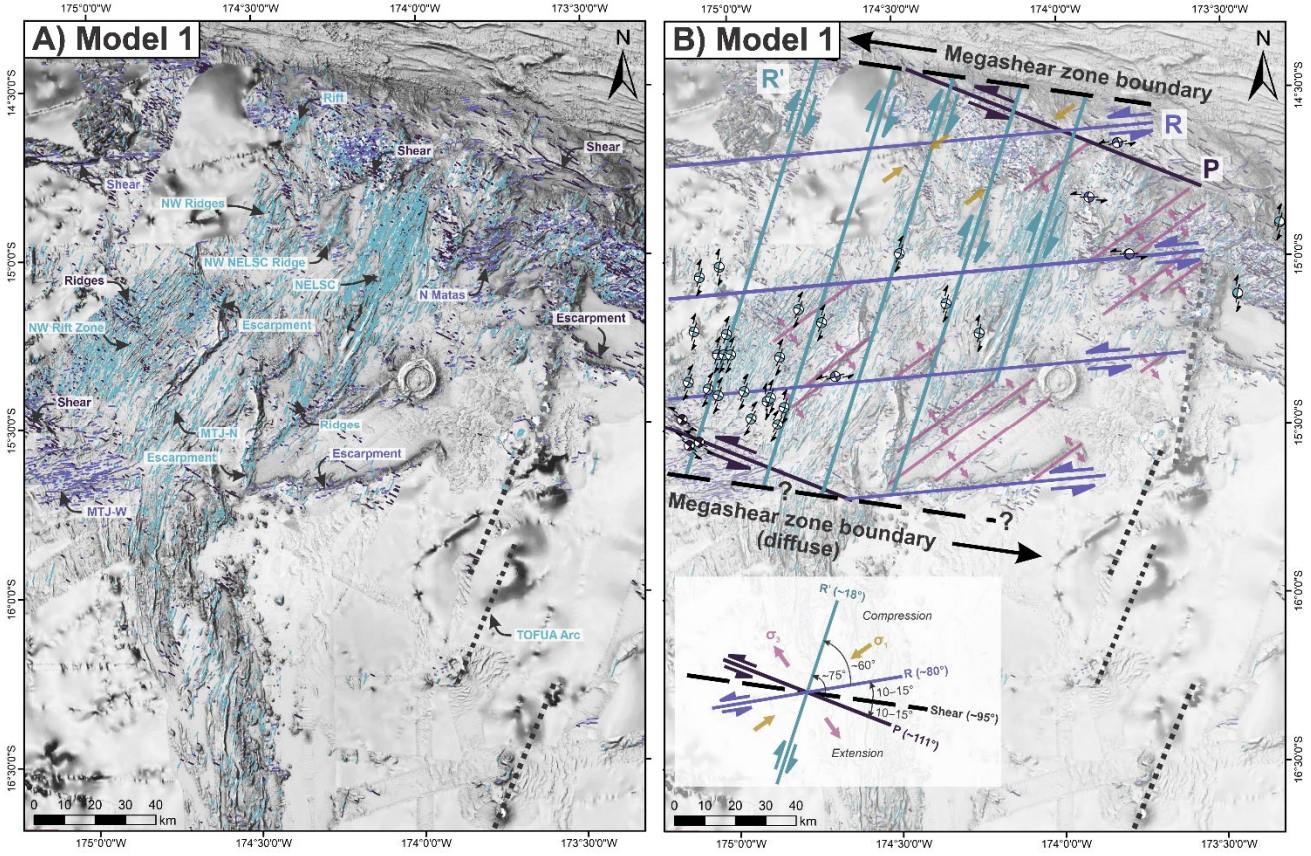

979

980 **Figure 9.** The first set of structures overlain on TTS-shaded bathymetry: (a) lineaments include NNE-
981 trending (~18°), E-trending (~80°), and WNW-trending (~111°), and are associated with numerous
982 major structural and volcanic features in the map area (annotations as in **Figure 2**); (b) generalized
983 megashear mechanism for this set of structures (Model 1), with shear zone boundaries oriented ~98°,
984 dominated by NNE-trending R′-shears (R-lateral) that are parallel to the southern Tofua Arc segments.
985 Extension associated with σ_3 is offset by R-shears (L-lateral) and is also associated with large volcanic
986 ridges across the map. Active seismicity (CMTs) is mainly restricted to the western map area,
987 extending south to a diffuse boundary (dashed line).

This is a provisional file, not the final typeset article

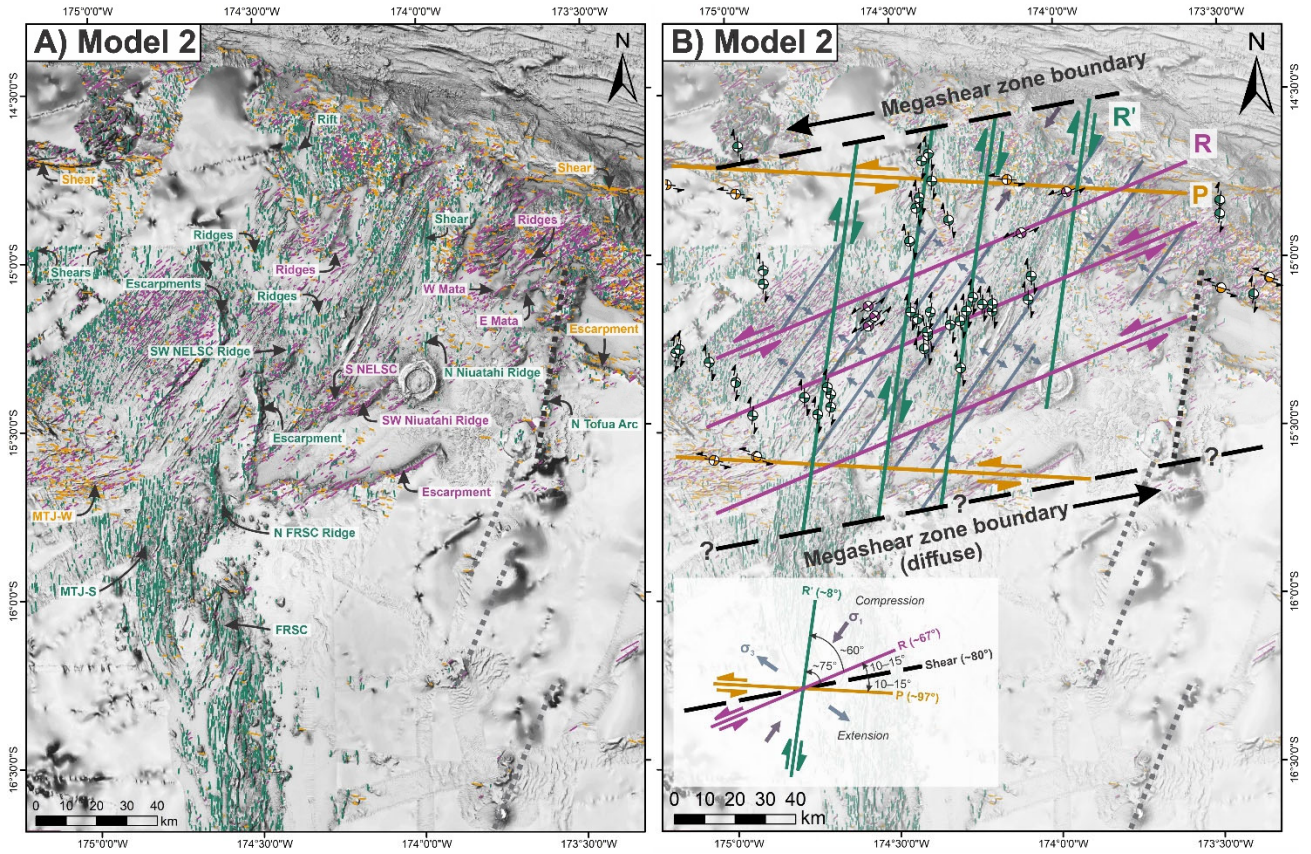

Figure 10. The second structure set overlain on TTS-shaded bathymetry: (a) lineaments include N-trending (~8°), ENE-trending (~67°), and W-trending (~97°), and are associated with numerous major structural and volcanic features in the map area (annotations as in **Figure 2**); (b) generalized megashear mechanism for this set of structures (Model 2), with shear zone boundaries rotated counter-clockwise to ~80°, dominated by N-trending R′-shears (R-lateral) that are parallel to the northern Tofua Arc segment. Extension associated with σ_3 is offset by R-shears (L-lateral) and is also associated with large volcanic ridges across the map. Active seismicity (CMTs) dominates the central map area closer to the arc, extending south to a diffuse boundary (dashed line).

Tables

Table 1. Cross-cutting relationships of structures according to orientation and interpreted Riedel association

Structure by Orientation	Riedel Model	Cross-Cuts	Cross-Cut by	Shear Sense
NNE-trending	Model 1 R'-shear	Model 1 P-shear	Model 1 R-shear, Model 2 R-shear	R-lateral
E-trending	Model 1 R-shear	Model 1 R'-shear, Model 1 P-shear	None	L-lateral
WNW-trending	Model 1 P-shear	None	Model 1 R'-shear, Model 1 R-shear, Model 2 R'-shear	Unknown
N-trending	Model 2 R'-shear	Model 1 P-shear, Model 2 -P-shear	Model 2 P-shear	R-lateral
ENE-trending	Model 2 R-shear	Model 1 R'-shear, Model 1 P-shear, Model 2 P-shear	None	L-lateral
W-trending	Model 2 P-shear	Model 2 R'-shear	Model 2 R'-shear, Model 2 R-shear	L-lateral